The Planetary Science Journal, 2:230 (18pp), 2021 December https://doi.org/10.3847/PSJ/ac2dfb

Evolution of Mercury's Earliest Atmosphere

Noah Jäggi[1], Diana Gamborino[1], Dan J. Bower[2], Paolo A. Sossi[3], Aaron S. Wolf[4], Apurva V. Oza[1,5], Audrey Vorburger[1], André Galli[1], and Peter Wurz[1]
[1] Physics Institute, University of Bern, Sidlerstrasse 5, 3012 Bern, Switzerland; noah.jaeggi@space.unibe.ch
[2] Center for Space and Habitability, University of Bern, Gesellschaftsstrasse 6, 3012 Bern, Switzerland
[3] Institute of Geochemistry and Petrology, Department of Earth Sciences, ETH Zurich, Clausiusstrasse 25, 8092 Zurich, Switzerland
[4] Earth and Environmental Sciences, University of Michigan, 1100 North University Avenue, Ann Arbor, MI 48109-1005, USA
[5] Jet Propulsion Laboratory, California Institute of Technology, Pasadena, CA 91109, USA
Received 2021 March 26; revised 2021 October 5; accepted 2021 October 7; published 2021 November 17

Abstract

MESSENGER observations suggest a magma ocean formed on proto-Mercury, during which evaporation of metals and outgassing of C- and H-bearing volatiles produced an early atmosphere. Atmospheric escape subsequently occurred by plasma heating, photoevaporation, Jeans escape, and photoionization. To quantify atmospheric loss, we combine constraints on the lifetime of surficial melt, melt composition, and atmospheric composition. Consideration of two initial Mercury sizes and four magma ocean compositions determines the atmospheric speciation at a given surface temperature. A coupled interior–atmosphere model determines the cooling rate and therefore the lifetime of surficial melt. Combining the melt lifetime and escape flux calculations provides estimates for the total mass loss from early Mercury. Loss rates by Jeans escape are negligible. Plasma heating and photoionization are limited by homopause diffusion rates of $\sim 10^{6}$ kg s^{-1}. Loss by photoevaporation depends on the timing of Mercury formation and assumed heating efficiency and ranges from $\sim 10^{6.6}$ to $\sim 10^{9.6}$ kg s^{-1}. The material for photoevaporation is sourced from below the homopause and is therefore energy limited rather than diffusion limited. The timescale for efficient interior–atmosphere chemical exchange is less than 10,000 yr. Therefore, escape processes only account for an equivalent loss of less than 2.3 km of crust (0.3% of Mercury's mass). Accordingly, $\leqslant$0.02% of the total mass of H_2O and Na is lost. Therefore, cumulative loss cannot significantly modify Mercury's bulk mantle composition during the magma ocean stage. Mercury's high core:mantle ratio and volatile-rich surface may instead reflect chemical variations in its building blocks resulting from its solar-proximal accretion environment.

Unified Astronomy Thesaurus concepts: Mercury (planet) (1024); Solar system terrestrial planets (797); Planetary atmospheres (1244); Planetary science (1255); Atmospheric composition (2120); Upper atmosphere (1748)

1. Introduction

MESSENGER data from X-ray, gamma-ray, and neutron spectrometers constrain the composition of Mercury's surface and motivate theories and models to understand Mercury's bulk composition, formation, and evolution. The surface composition and geology of Mercury are compatible with partial melting of cumulates that were originally formed by magma ocean crystallization (McCoy et al. 2018). Subsequent impact excavation exposed the cumulates at the surface (McCoy et al. 2018; Charlier et al. 2013). The low oxygen fugacity (fO_2) of the uppermost layer of Mercury's regolith, together with Mercury's large core size, suggests a reduced mantle where nominally lithophile elements such as Ca, Mn, Cr, and Ti are present in sulfides rather than silicates (Vander Kaaden & McCubbin 2016). Relative to basaltic rocks exposed at the surface of other terrestrial planets, a large amount of the moderately volatile element Na (3–5 wt%) is detected on Mercury's surface (Peplowski et al. 2014). Observations of Na variation in Mercury's exosphere may relate to nightside deposit formation and dawn reemission (e.g., Cassidy et al. 2016). Hence, it remains an open question how moderately volatile elements such as Na may have accumulated on the surface—whether from an extant or now-extinct process—and how their abundance compares to Mercury's bulk composition.

Magma oceans are pivotal in determining the initial conditions and subsequent evolution and chemical differentiation of terrestrial planets in the solar system (e.g., Elkins-Tanton 2012; Chao et al. 2021). Radiometric dating reveals that magmatic iron meteorites, which represent planetesimal cores, formed within 2 Myr of solar system formation (Kruijer et al. 2014). The rocky planet whose mass is most similar to that of Mercury, and for which samples are available, Mars, likely accreted, formed an iron core, and underwent complete solidification of its magma ocean within about 20 Myr of solar system formation (Bouvier et al. 2018). Crucially, rapid core formation in terrestrial planets requires a magma ocean to enable efficient metal segregation (Stevenson 1990). By analogy, and given its solar-proximal location, extensive melting is therefore expected to have occurred on proto-Mercury (Brown & Elkins-Tanton 2009; Vander Kaaden & McCubbin 2016). Following its crystallization, partial melting of magma ocean cumulates has been invoked to explain Mercury's contemporary surface composition (McCoy et al. 2018).

Energy from accretion and radiogenic heat (e.g., from ^{26}Al) may have driven the differentiation of Mercury if it formed sufficiently early in solar system history (Siegfried & Solomon 1974; Bhatia & Sahijpal 2017). Following a phase of rapid growth, the subsequent reduction of impactor flux would have enabled Mercury's magma ocean to cool and crystallize without additional large-scale remelting. During this

time, the mantle is expected to have stratified into a basal layer of olivine and a plagioclase- and clinopyroxene-dominated crust, which is now observed on Mercury's surface (Brown & Elkins-Tanton 2009). During the cooling of the magma ocean when the surface remains mostly molten, chemical species readily exchange between the interior, atmosphere, and exosphere—as occurred for other terrestrial planets in the solar system (e.g., Elkins-Tanton 2008).

Fegley & Cameron (1987) addressed the hypothesis that the anomalously high bulk density of Mercury (owing to a high core/mantle ratio) is the result of evaporation of silicate melt components from the surface of a Hermean magma ocean. They presumed that atmospheric loss was sufficiently slow that the atmosphere remained in equilibrium with the magma ocean. In their model, vapor was removed in a stepwise fashion and the composition of the magma ocean evolved accordingly. In reality, however, evaporated species are transported, mixed, and lost from the atmosphere and exosphere, with the flux at which loss occurs integrated over the magma ocean lifetime ultimately dictating the total mass loss. Therefore, consideration of interior, atmospheric, and exospheric processes is necessary to assess whether significant quantities of rock-derived atmospheres can be lost during the Hermean magma ocean stage.

Based on observations of solar-mass stars, the early solar extreme-ultraviolet (EUV) and X-ray fluxes were likely 400 times larger than they are today. This would have made photoionization a highly efficient nonthermal—and photoevaporation a highly efficient thermal—atmospheric escape mechanism (Johnstone et al. 2015; Tu et al. 2015). Other loss mechanisms of potential importance include atmospheric sputtering and kinetic escape (e.g., Jeans escape) that occur over the lifetime of the magma ocean. Nonthermal loss rates can be constrained by known plasma pressures at proto-Mercury owing to the incoming solar wind, as well as EUV luminosities of the early Sun estimated from population studies of nearby Sun-like stars (Ribas et al. 2014; Tu et al. 2015).

In this paper we establish the extent of element evaporation and loss from Mercury during its early magma ocean phase. Models are constructed of (1) the coupled evolution of the magma ocean and atmosphere, (2) the evaporation of metals and metal oxide species from the Hermean magma ocean, (3) the mixing ratios and abundances of molecular species throughout the atmosphere and at the exobase, and finally (4) loss rates of these species from the upper atmosphere. We discuss these results in the context of the chemical evolution of Mercury's surface environment, bulk composition, and present-day observations.

2. Method

2.1. Overview

Our combined modeling strategy provides insight into the initial composition and evolution of Mercury's exosphere by considering (1–2) energy and mass exchange between the interior and atmosphere, (3) speciation in the atmosphere, and (4–5) loss from the exosphere:

1. SPIDER (Bower et al. 2018, 2019, 2021) is a coupled interior–atmosphere model used to determine the surface temperature and lifetime of melt at the surface, as well as the pressure–temperature structure of the atmosphere. Magma ocean cooling is regulated by the atmospheric opacity, which depends on the pressure of atmospheric species and hence the solubility of species in melt.
2. VapoRock calculates the equilibrium partial pressures of metal-bearing gas species of the elements Si, Al, Mg, Ca, Na, Fe, and K above the magma ocean surface (Wolf et al. 2021). This determines the metal-bearing composition of the atmosphere as a function of temperature and the bulk composition of the magma ocean. It utilizes ENKI's ThermoEngine (http://enki-portal.org) and combines estimates for element activities in silicate melts with thermodynamic data for metal and metal oxide vapor species (Lamoreaux & Hildenbrand 1984; Lamoreaux et al. 1987).
3. VULCAN (Tsai et al. 2017, 2021) solves for the equilibrium chemistry of the atmosphere as a function of altitude by using element abundances for metals (output by VapoRock), volatile abundances (output by SPIDER), and the atmospheric pressure–temperature structure (also output from SPIDER). This provides the mixing ratios of atmospheric species, which are required to calculate escape at the exobase.
4. DISHOOM (Oza et al. 2019; Gebek & Oza 2020) is an atmospheric evolution model that computes the total mass loss of gaseous species to space due to ultraviolet (EUV) heating, surface heating, and plasma heating.
5. The Exospheric Monte Carlo (E-MC) model (Wurz & Lammer 2003; Vorburger et al. 2015; Gamborino et al. 2019) determines the rate of exospheric escape of particles due to Jeans escape and photoionization. It tracks particle trajectories using a thermal energy distribution that depends on the temperature at the exobase.

2.2. Cooling of the Magma Ocean

Previous thermal modeling of Mercury's interior has focused either on the accretion phase (Bhatia & Sahijpal 2017) or on its long-term evolution over billions of years (e.g., Stevenson et al. 1983; Spohn 1991; Grott et al. 2011; Tosi et al. 2013). Here, we model the thermal evolution of Mercury's magma ocean at the end of its accretion phase. At this time, the final magma ocean cools and crystallizes on a timescale short enough that there is negligible disruption so that our results remain independent of its accretion history. We model the thermal evolution of Mercury's magma ocean using SPIDER (Bower et al. 2018, 2019) to constrain the duration of melt at the surface as it cools from 2400 to 1500 K. This is necessary to compute the evaporation of metals and metal oxides at the planetary surface, prior to the formation of a surface lid around 1500 K. Heating by the decay of radiogenic isotopes ^{26}Al, ^{40}K, ^{232}Th, ^{235}U, and ^{238}U is included in our model, and the model starts from solar system time zero to obtain an upper estimate of the surface cooling time. The main parameters are provided in Table A1 (Appendix A) and are guided by the parameters and results from previous models of Mercury (Bhatia & Sahijpal 2017; Tosi et al. 2013).

Cases prefixed by "S" ("small Mercury"; Table 1) have a planetary radius of 2440 km, which is the present-day radius of Mercury. Cases prefixed by "L" have a radius of 3290 km, which assumes that Mercury was larger than at present day, perhaps due to mantle stripping driven by an impactor (Benz et al. 2008; Asphaug & Reufer 2014; Chau et al. 2018). Cases with "V" (volatile) consider the partitioning of carbon and

Table 1
Parameters for the Magma Ocean Cases

Case	R_P (km)	g (m s^{-2})	H_2O	H_2	CO_2	CO	SiO
			Pressure (bar) at 2000 K				
SN5	2440	3.7	⋯	⋯	⋯	⋯	$1.4E-4$
SN3	2440	3.7	⋯	⋯	⋯	⋯	$1.4E-4$
SV	2440	3.7	0.7	3.2	0.05	1.1	⋯
LN5	3290	4.0	⋯	⋯	⋯	⋯	$1.4E-4$
LN3	3290	4.0	⋯	⋯	⋯	⋯	$1.4E-4$
LV	3290	4.0	1.2	5.8	0.2	4.9	⋯

Note. Small (S) and large (L) Mercury models are inspired by models M1 and M4 from Bhatia & Sahijpal (2017), respectively. The second letter of the case name denotes with volatiles (V) and no volatiles (N). Nonvolatile cases have an additional number of either 5 or 3, to denote small (10^{-5} m^2 kg^{-1}) and large (10^{-3} m^2 kg^{-1}) SiO opacity, respectively (Semenov et al. 2003).

hydrogen species, here termed volatiles, between the melt and atmosphere, as well as redox reactions (Bower et al. 2021). By contrast, cases with "N" (nonvolatile) do not consider volatiles but rather assume that SiO is the only IR absorbing species; a suffix of "5" denotes a low SiO opacity (10^{-5} m^2 kg^{-1}), and a suffix of "3" denotes a large SiO opacity (10^{-3} m^2 kg^{-1}), both at a reference pressure of 3×10^{-6} bar (Figure 2 in Semenov et al. 2003). For nonvolatile cases, the surface pressure of SiO is imposed in SPIDER as a function of surface temperature as determined by VapoRock calculations. Then, the atmospheric opacity and hence magma ocean cooling rate can be determined.

For cases SV and LV, carbon and hydrogen can exist as either reduced (CO, H_2) or oxidized (CO_2, H_2O) species, where the fO_2 is constrained to one log unit below the iron-wustite buffer ($\Delta IW = -1$, IW-1 hereafter). This is marginally higher than the most recent estimates for the fO_2 of Mercury's mantle (Cartier & Wood 2019). For cases SV and LV, we determine the total H and C abundances by calculating the ppmw necessary for an Earth-size planet to produce a 100 bar CO_2 (i.e., Venus-like atmosphere) and 270 bar H_2O (i.e., one Earth ocean mass) atmosphere. The abundances of H and C are equivalent to 330 ppmw of H_2O and 120 ppmw of CO_2, respectively. The mass of large Mercury's mantle is about a factor of 5 larger than small Mercury's mantle, resulting in a 5 times increase in the total volatile budget.

2.3. Evaporation from the Magma Ocean

At the high surface temperatures that characterize a magma ocean (>1500 K), the partial pressures of the vapor species of the major rock-forming oxides (e.g., SiO_2, $NaO_{0.5}$, $KO_{0.5}$) can become significant (Visscher & Fegley 2013; Sossi & Fegley 2018; Sossi et al. 2019). Gas-liquid equilibria for these elements are described by congruent evaporation, generalized as

$$M^{x+n}O_{(x+n)/2}(l) = M^xO_{x/2}(g) + \frac{n}{4}O_2(g), \quad (1)$$

where M is the metal, x is the oxidation state of the metal in its gaseous state, and n is the number of electrons exchanged in the reaction. Both x and n are integer values that may be $\geqslant 0$ or $\leqslant 0$. At equilibrium, the partial pressure of any given metal or metal oxide species in an ideal gas is given by

$$p(M^xO_{x/2}) = \frac{K_{(1)}X(M^{x+n}O_{(x+n)/2})\gamma(M^{x+n}O_{(x+n)/2})^{(n/4)}}{(fO_2)}, \quad (2)$$

where $K_{(1)}$ is the equilibrium constant of the reaction (Equation 1), X is the mole fraction, and γ is the activity coefficient of the metal oxide melt species, $M^{x+n}O_{(x+n)/2}$. Equilibrium constants involving 31 gas species (Table B2, Appendix B) are calculated according to their thermodynamic properties given in Lamoreaux et al. (1987) and Lamoreaux & Hildenbrand (1984). Evident from Equation (2) is that estimates for the composition of the silicate melt in addition to the activity coefficients of its constituent components are required to correctly predict partial pressures. To this end, likely compositions representative of Mercury's crust, mantle, and possible precursors are shown in Table 2. The MELTS algorithm is used to estimate activity coefficients of melt oxide species (Ghiorso & Sack 1995). The fO_2 is constrained to lie one log unit below the IW buffer (IW-1), which is calculated according to O'Neill & Eggins (2002):

$$\log fO_2(IW) = 2\frac{-244118 + 115.559\,T - 8.474\,T\ln(T)}{\ln(10)RT}, \quad (3)$$

where T is temperature and R the gas constant. These ingredients together comprise the VapoRock code and permit calculation of equilibrium partial pressures over a range of temperatures, fO_2, and silicate melt compositions (Wolf et al. 2021).

Table 2
Magma Ocean Surface Composition

Oxide (wt%)	EH4	CB	NSP Source	NSP Lava
SiO_2	62.73	50.70	53.67	58.70
Al_2O_3	2.58	4.60	4.75	13.80
MgO	30.24	36.90	36.89	13.90
CaO	1.99	3.30	2.26	5.81
FeO	0.00	3.50	0.02	0.04
Na_2O	1.71	0.19	1.97	7.00
K_2O	0.20	0.05	0.05	0.20
Total	99.45	99.24	99.61	99.45

Note. Compositions based on enstatite chondrites (EH4; Wiik 1956); CB chondrite chondrule data with bulk CB Na and K mass balanced for chondrules to fit bulk meteorite iron-silicate ratio (Weisberg et al. 2000, 1990; Lauretta et al. 2007); and northern smooth plains (NSP) composition for the lava and source (Namur et al. 2016; Nittler & Weider 2019).

2.4. Magma Ocean Composition

The composition of the early Hermean mantle is uncertain. To address how variability in the surface composition affects the evolved partial pressures of metal and metal oxide gas species, four compositions are investigated (Table 2): (1) enstatite chondrites (EH4), (2) Bencubbin chondrites (CB), (3) northern smooth plain (NSP) lava, and (4) NSP source. The first composition assumes that core–mantle differentiation was sluggish, with the composition of the magma ocean being approximated by enstatite chondrites (EH4), often cited as

Table 3
Surface Element Ratios at $T_{surf} = 2000$ K

Composition	Element Ratios						
	C/H	O/H	Mg/H	Si/H	Na/H	K/H	Fe/H
SV Case							
EH4	1.532E-01	2.472E-01	1.251E-06	1.469E-05	1.254E-04	1.121E-05	1.053E-08
CB			1.680E-06	1.039E-05	7.155E-05	5.785E-06	9.388E-06
NSP source			1.740E-06	1.020E-05	2.282E-04	5.254E-06	7.155E-07
NSP melt			9.642E-07	1.161E-05	3.480E-04	7.139E-06	1.351E-06
LV Case							
EH4	3.608E-01	4.641E-01	6.806E-07	7.997E-06	6.825E-05	6.104E-06	5.732E-09
CB			9.144E-07	5.653E-06	3.894E-05	3.148E-06	5.109E-06
NSP source			9.469E-07	5.551E-06	1.242E-04	2.859E-06	3.894E-07
NSP melt			5.248E-07	6.321E-06	1.894E-04	3.886E-06	7.354E-07

Note. Ratios are based on SPIDER and VapoRock results for magma ocean compositions given in Table 2. We neglect Al and Ca, as their vapor pressures do not exceed 10^{-9} bar at 2000 K for any composition.

appropriate starting compositions for Mercury owing to their high bulk iron content, strongly reduced nature, and the resemblance of partial melts thereof to Hermean surface compositions (Nittler et al. 2011). We assume that all FeO is extracted in the form of metallic iron to form Mercury's core, which results in high SiO_2 and MgO contents in the complementary silicate fraction.

The second composition is based on chondrules found in the Bencubbin class of carbonaceous chondrites (CB), which best reproduce Mercury's surface composition based on MESSENGER data (Brown & Elkins-Tanton 2009; McCoy et al. 2018). Spectrometric measurements of Mercury's surface show a crust rich in Na and S and poor in Fe relative to other basaltic rocks (Nittler & Weider 2019). Presuming that these abundances are representative of bulk Mercury, two other compositions are investigated: the NSP lava (NSP melt) that represents a volatile-rich composition observed on the surface, and its inferred mantle source (NSP source; Nittler & Weider 2019). These two compositions represent Mercury's crust and mantle, respectively. Although it is not anticipated that magma ocean crystallization produced the NSP melt composition directly, it is included to define an end-member opposing the CB composition that is Na and K poor and comparably Fe-rich (Table 2).

2.5. Atmospheric Structure

The atmospheric structure is constrained by the temperature at the magma ocean–atmosphere interface, the planetary equilibrium temperature, and the atmospheric composition and pressure (Appendix E). For nonvolatile cases, the calculated vapor pressures of Si, Na, K, Fe, Mg, Al, and Ca oxide species in equilibrium with the magma ocean (Figure 2) are used directly in the exospheric loss model (Section 2.6). SiO vapor pressures reported in Table 1 at $T_{surf} = 2000$ K are not strongly affected by the magma ocean composition and are in the range of $10^{-4\pm0.1}$ bar. For cases SV and LV in which Mercury's atmosphere contains outgassed H- and C-bearing gases, the partial pressures of H_2, H_2O, CO, and CO_2 are calculated by SPIDER according to volatile solubility and fO_2 buffered by the magma ocean at IW-1. A modified version of the VULCAN code is then used to compute the equilibrium chemical speciation in the atmosphere that contains both the metal-bearing gases and H and C volatiles (Tsai et al. 2017, 2021). VULCAN computes the atmospheric mixing ratios using the pressure–temperature (P–T) structure of the atmosphere.

VULCAN by default includes about 300 reactions for C, H, O, and N, to which we added reactions involving Si, Mg, Ca, Fe, Na, and K to obtain their equilibrium speciation (Table C3, Appendix C). Table 3 shows the initial element-to-hydrogen ratios used in the VULCAN calculations. Surface vapor pressures of Ca- and Al-bearing species did not exceed 10^{-6} bar in the magma ocean temperature range investigated and are thus excluded. For the remaining species we used a case-dependent P–T profile from SPIDER at a surface temperature of 2000 K to determine the mixing ratio of species in the atmosphere as a function of altitude. The P–T profile may imply condensation of certain elements initially present in the vapor, which may rain out of the atmosphere prior to escape. To assess this possibility, Gibbs free energy minimization of the atmospheric composition was performed throughout the atmospheric column using FactSage 7.3 (Bale 2016).

SPIDER and, for volatile cases, VULCAN provide descriptions of the atmospheric structure and composition needed to determine the altitude of the homopause and exobase. The homopause is the altitude at which molecular diffusion exceeds diffusion by eddies and thus separates the well-mixed lower atmosphere from the mass-separated upper atmosphere. The exobase is the altitude at which gas is loosely bound to the planet and is collisionless (Knudsen number = 1), resulting in efficient escape.

2.5.1. Homopause Level and Diffusion

To determine the homopause level z_{hom}, we require the particle density at the homopause n_{hom}. For a steady-state homopause height, the molecular coefficient D_{ik} is equal to the eddy diffusion coefficient K_{zz}, allowing us to solve for the particle density n_{hom}. The diffusion coefficient D_{ik} ($m^2\,s^{-1}$) within the homosphere is calculated for each major species using the Chapman−Enskog relation (Chapman & Cowling 1970). It determines the binary diffusion rate of a gaseous species i with mass m_i within a gas of average mass m_k:

$$D_{ik} = \frac{3\sqrt{k_B T_{skin}}}{8 n_{hom} \sigma_{ik}^2 \Omega_{ik}} \sqrt{\frac{1}{2\pi}\frac{m_i + m_k}{m_i m_k}}, \quad (4)$$

where k_B is the Boltzmann constant and $T_{\rm skin}$ the absolute temperature at the homopause (skin temperature). Homopause pressures ($P_{\rm hom} = n_{\rm hom} k_B T_{\rm skin}$) for each species are thereby about 10^{-6} bar for all cases. We approximate the intermolecular distance $\sigma_{ik} = \frac{\sigma_i + \sigma_k}{2}$ with the radius of the species relative to the mean species diameter weighted by the mixing ratio. The dimensionless collision integral Ω_{ik} is assumed to be unity.

The eddy velocity is often approximated by the atmospheric species thermal speed $v_{\rm th}$, and the characteristic eddy length scale $L_{\rm eddy}$ is approximated by the atmospheric scale height H (e.g., Atreya et al. 1986). Values for $K(z) = v_{\rm eddy} L_{\rm eddy}$ that are calculated based on this assumption exceed the suggested eddy diffusion coefficient upper limit of 320 $\rm m^2\ s^{-1}$ by several orders of magnitude (Vlasov & Kelley 2015). Hence, we use this upper limit in the volatile cases to determine $n_{\rm homo}$, which is based on the energy dissipation rate within Earth's atmosphere.

To compute the $z_{\rm hom}$ and $T_{\rm hom}$ for the volatile cases, we determine the altitude at which the P–T profile reaches a number density $n_{\rm homo}(K(z))$. As the number density at the homopause only depends on K_{zz} with the same order of magnitude for both volatile and nonvolatile cases, $n_{\rm homo}(K(z))$ is approximately 10^{18}–10^{19} at $\rm m^{-3}$. For the nonvolatile cases we do not obtain a $P(z)$–T profile from VULCAN for the nonvolatile cases owing to the absence of H-based species. We therefore use the barometric formula with gravity as a function of height to compute $z_{\rm hom}$.

2.5.2. Exobase Level

Due to the large difference in number density between the homopause and the exobase, the barometric formula is not applicable assuming an isothermal upper atmosphere with height-dependent gravity. We approximate the exobase height of early Mercury, which is subject to extensive loss, by finding an exobase height that results in a loss rate that is in equilibrium with the homopause diffusion rate. The loss from the exobase is proportional to the exobase height (increasing surface area), whereas diffusion from the homopause to the exobase is inversely proportional to the exobase height (decreasing density gradient). The exobase altitude $z_{\rm exo}$ of each species is determined for all cases by setting the homopause diffusion rate $\dot{M}_{{\rm diff},i}$ equal to the largest, diffusion-limited mass-loss rate of photoionization $\dot{M}_{\rm ion}$ (Equation (9), Section 2.6).

The homopause diffusion rate $\dot{M}_{\rm diff}$ in $\rm kg\ s^{-1}$ of a species i is obtained by multiplying the diffusion coefficient D_{ik} by the species number density gradient, the species mixing ratio at the homopause $n_i/n_{\rm hom}$, and the homopause surface area $A_{\rm hom}$:

$$\dot{M}_{{\rm diff},i} = -D_{ik} \frac{\Delta n_{\rm exo-hom}}{\Delta z_{\rm exo-hom}} m_i \frac{n_i}{n_{\rm hom}} A_{\rm hom}. \quad (5)$$

The number density of particles at the exobase $n_{\rm exo}$ is necessary to determine the number density gradient between the homopause and exobase and ultimately $z_{\rm exo}$. For a single species i, the exobase is defined at an altitude at which the particle free path ($\lambda_{\rm col} = 1/n_{\rm exo}\sigma_{\rm col}$) is equal to the exospheric scale height ($H = k_B T/mg$), and therefore (i.e., Gronoff et al. 2020)

$$n_{i,{\rm exo}} = \frac{1}{H_i \sigma_i} = \frac{m_i\, g(h)}{k_B\, T_{\rm skin}\, \sigma_i}, \quad (6)$$

with the collision cross section (CCS) σ_i, the skin temperature $T_{\rm skin}$, and the acceleration of gravity $g(h)$ at the exobase altitude $z_{\rm exo}$. In a multispecies atmosphere, each species has a specific mass and CCS, leading to a species-specific scale height and exobase density and altitude. The CCSs of each species are approximated as their respective atom or molecule size (Table D4, Appendix D). Typical values for $n_{\rm exo}$ are around 10^{12}–10^{13} atoms $\rm m^{-3}$, which coincides with $\sim 10^{-12}$ bar. The skin temperature used for determining $z_{\rm exo}$ and $z_{\rm hom}$ is derived from the atmosphere model (Appendix E):

$$T_{\rm skin} = \left[\frac{\epsilon\,(T_{\rm surf}^4 - T_\infty^4)}{2} + T_\infty^4 \right]^{1/4}, \quad (7)$$

with the magma ocean surface temperature $T_{\rm surf}$, emissivity ϵ (depends on optical depth and hence atmospheric composition and pressure), and equilibrium temperature T_∞.

2.6. Exospheric Loss

The E-MC escape model focuses on Jeans escape, photoionization, and photodissociation to investigate the loss of proto-Mercury's exosphere. These mechanisms compete for importance; Jeans escape acts at high exospheric temperatures, whereas photoionization and photodissociation act at large solar EUV and X-ray fluxes present during early times, respectively. The E-MC model simulates escape by tracking $\sim 10^5$ exospheric particles, with trajectories initiated at the exobase with a random angle and energy selected from a Maxwellian velocity distribution function (Vorburger et al. 2015). The initial energy of the exospheric particles depends on the exobase temperature, which decreases with time owing to magma ocean and atmospheric cooling.

The loss processes in the E-MC model are calculated on a particle-by-particle basis. As soon as a particle reaches Mercury's Hill radius (Table 4), it is assumed to have escaped Mercury's gravitational attraction and is subsequently removed from the simulation. Another loss process is through interaction with photons. At each altitude step starting from the exobase and moving away from the planet, the E-MC model calculates the probability of a particle being photodissociated or photoionized. If the particle is photodissociated, the code calculates the corresponding trajectories of the fragments and assesses the chance of escaping the gravitational well and the potential for subsequent photoionization. Ionized particles are considered lost from the exosphere, assuming they are picked up by the electromagnetic forces of the solar wind plasma or Mercury's magnetospheric plasma. Photoionization and photodissociation rates are scaled for each dominant species using the EUV flux of the early Sun. The EUV flux and mass loss are dependent on the rotational evolution of the Sun, with a fast rotator being much more active than a slow rotator (Johnstone et al. 2015; Tu et al. 2015). We consider a moderately fast rotating Sun, where the EUV luminosity $L_{\rm EUV}$ ($\rm J\ s^{-1}$) is

$$L_{\rm EUV} = (4.7 \times 10^{25})\, t^{-1.18}, \quad (8)$$

where t (Ma) is the time since the formation of the solar system. Typical values for the incident EUV fluxes at Mercury at 1 and 5 Ma are thereby $10^{3.0}$ and $10^{2.2}$ $\rm J\ s^{-1}\ m^{-2}$, respectively.

The loss is equal to the sum of the exospheric particles that have been either photoionized or lost through gravitational escape. The loss of a given species from the exosphere at a given time is then calculated using its mixing ratio at the exobase. For a given exobase temperature, the loss rate ($\dot{M} = dm/dt$) from the

Table 4
Escape Parameters λ_0 for Small Mercury and Large Mercury Cases at $T_{surf} = 2000$ K

Species	λ_0	μ_{atm} (amu)	T_{exo} (K)	z_{exo} (km)	Case
Small Mercury, $R_H = 72\ R_P$					
Na, K, Fe	7.8	24.1	1613	2670	SN5, SN3
H, C, O	7.6	14.3	1021	2370	SV
Large Mercury, $R_H = 90\ R_P$					
Na, K, Fe	15.7	24.1	1615	1890	LN5, LN3
H, C, O	15.3	14.3	893	2160	LV

Note. The escape parameter λ_0 with the respective mean molecular weight of the upper atmosphere μ_{atm}, as well as the exobase temperature T_{exo} and altitude z_{exo}. The Hill radius R_H in Mercury radii R_P describes the gravitational field of influence of Mercury in each case.

exosphere by photoionization $\dot{M}_{ion}$ is

$$\dot{M}_{ion} = \sum_{i=0} \psi_i^{source}\ \xi_i\ m_i A_{exo}, \tag{9}$$

where A_{exo} is the surface area of the exobase and $0 \leqslant \xi_i \leqslant 1$ is the fraction of lost particles of a species i with mass m_i, thermal speed of v_i^{therm}, and particle flux leaving the exobase of $\psi_i^{source} = n_i^{exo}\ v_i^{therm}$. The area of the exobase is equal to sum of the R_P and z_{exo} (Section 2.5). The total loss is determined by integrating the loss flux over the lifetime of surficial melt.

2.7. Atmospheric Loss and Surface Evaporation

Atmospheric loss by thermal processes (photoevaporation) and nonthermal processes (plasma heating) is determined using DISHOOM (Oza et al. 2019), using Equation (10) and Equation (11), respectively. Preliminary calculation of Jeans escape using DISHOOM demonstrated negligible loss due to surface heating compared to all other mechanisms. The escape parameters appropriate to proto-Mercury are summarized in Table 4.

Irradiation from the impinging solar wind plasma and high-energy photons may heat the atmosphere and drive escape at a level that is significantly larger than surface heating and photoionization. Upper atmospheric heating (photoevaporation) is caused by incoming X-ray and EUV photons that deposit heat into a neutral medium via molecular absorption (Watson et al. 1981) or photoelectric heating (Murray-Clay et al. 2009). This expands the atmospheric envelope beyond the gravitational influence of the body (R_H in Table 4). The heating can be estimated by energy-limited escape driven by EUV photons (Watson et al. 1981), which is a reasonable approximation to thermally driven hydrodynamic escape (Volkov & Johnson 2013; Krenn et al. 2021):

$$\dot{M}_U = \frac{\eta_{EUV}\ L_{EUV}\ 2\pi\ z_{abs}^2}{U_{env}}, \tag{10}$$

where z_{abs} is the absorption altitude, generally taken to be 1.25 planetary radii for an outgassing atmosphere (e.g., Johnson et al. 2015) where the X-ray and EUV photons can absorb and thereby deposit heat into the atmospheric molecules. We note that we use 1.25 Mercury radii R_P as a conservative lower limit in absorption altitude, as the homopause situated at $\sim$1.4 R_P represents an upper limit. The efficiency at which the atmosphere is heated, η_{EUV}, is uncertain, so we use 10^{-3} as a conservative lower estimate (Ito & Ikoma 2021) and 10^{-1} as an upper limit (Mordasini 2020). Both efficiencies that we used were previously applied to atmospheres that use vastly different planet parameters but similar enough, as they consider a metal oxide (nonvolatile) or an H/He (volatile) atmosphere, respectively. Hot Jupiter H/He envelopes, as well as volcanic atmospheres, suggest that η_{EUV} may be as large as 0.35 (Lellouch et al. 1992; Murray-Clay et al. 2009).

Mass loss due to plasma heating is observed at Jupiter's moon Io and is fundamentally driven by plasma ram pressure and magnetic pressure interacting with the atmosphere (e.g., Johnson 1990). Therefore, we estimate the atmospheric loss from an impinging plasma on Mercury by scaling to the plasma pressures measured at the Galilean satellites (Johnson 2004). Following Oza et al. (2019) and Gebek & Oza (2020), the mass loss of a species i by plasma heating at proto-Mercury is

$$\dot{M}_{P,i} = \frac{x_i}{\dot{M}_{i,Io}}\ \hat{P}\ \hat{U}\ \hat{v}_{ion}(\hat{h}_{exo})^2, \tag{11}$$

where x_i is the element fraction of the species i in the atmosphere and $\dot{M}_{i,Io}$ its atmospheric sputtering loss rate at Io. The total plasma pressure $\hat{P}$, gravitational binding energy $\hat{U}$, and ion velocity $\hat{v}_{ion}$ of Mercury are expressed as nondimensional values that are scaled to Io's corresponding values. The total plasma pressure is additive where $P_{tot} = P_{mag} + P_{ram}$. For the calculations we use a magnetic pressure $P_{mag} = 1.7$ nPa based on an estimation of Mercury's magnetic moment of 2.76×10^{12} T m^3 at the magnetopause standoff distance of 1.4 R_P. The ram pressure due to the solar wind varies from $\sim$10 to 30 nPa (Korth et al. 2012), yielding a total pressure of $\sim$12–32 nPa.

Evaporation from the magma ocean and atmospheric loss have to be equal to retain the atmospheric pressure and thus a steady state. The evaporation rate of a species is approximated by the Hertz–Knudsen–Langmuir equation. The evaporation rate of a species i with molar mass M_i over the surface of Mercury in mol s^{-1} is given by

$$\dot{M}_{evap,i} = M_i \frac{dn_i}{dt} = -4\pi R_P^2 M_i \frac{\gamma_{ev} P_{i,eq} - \gamma_{en} P_{i,s}}{\sqrt{2\pi M_i RT}}, \tag{12}$$

with the evaporation and condensation coefficients γ (set to unity for a liquid), surface pressure P_s, equilibrium pressure P_{eq}, and the Mercury radius R_P. By setting the homopause diffusion rate $\dot{M}_{diff,i}$ equal to the evaporation rate $\dot{M}_{evap,i}$, the equation is solved for the ratio of surface to equilibrium pressure, $p_{i,s}/p_{i,eq}$ for each species at each temperature step. For homopause diffusion rates, the ratio lies >0.99; therefore, the atmosphere up to the homopause is considered to be in equilibrium.

3. Results

3.1. Surficial Melt Lifetime and Atmospheric Structure

The surface temperature of the Hermean magma ocean cools from 2400 to 1500 K in around 400–9000 yr, depending on the planetary size (i.e., mantle mass) and efficiency of radiative

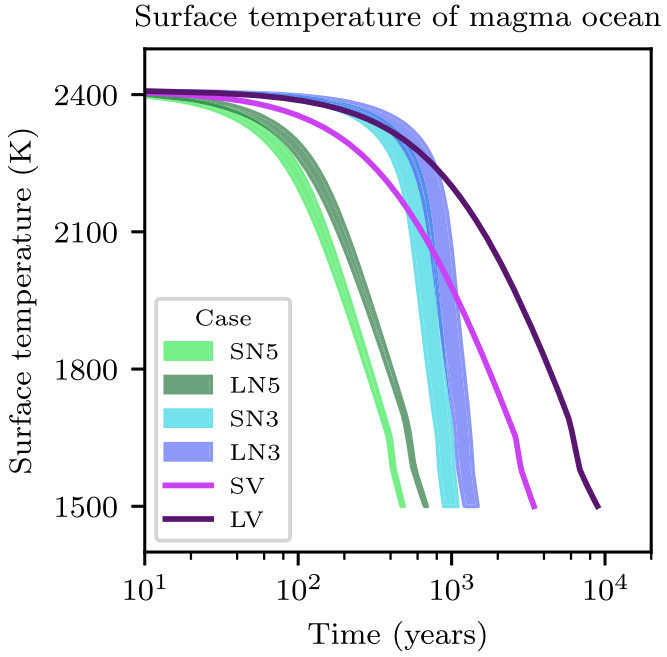

Figure 1. Evolution of the surface temperature of the Hermean magma ocean. For nonvolatile cases, the upper bound of cooling is provided by EH4 composition and the lower bound by Cb composition. See Table 1 for case parameters.

energy loss to space (Figure 1). The cooling rate is inversely proportional to R_P since it depends on the ratio of the planetary surface area to mantle mass. Hence, a large Mercury takes longer to cool than a small Mercury for otherwise-identical parameters.

3.1.1. Nonvolatile Cases

The cooling trajectory of nonvolatile cases is characterized by two episodes. First, when the surface temperature is high (early time), the pressure and hence opacity of SiO are large, and therefore cooling is slow. The second episode of cooling is rapid, since even a small decrease in surface temperature produces a drastic fall in both SiO pressure and opacity, driving the planet toward cooling like an ideal blackbody. Therefore, the cooling timescale for N5 cases is only marginally greater than for an ideal blackbody, which bounds the minimum cooling time to 470 yr. Increasing SiO opacity by 2 orders of magnitude increases the minimum cooling time to around 1000 yr (N3 cases), marginally affected by the chosen magma ocean composition.

Nonvolatile cases at 2400 K have thin atmospheres of <0.1 bar and comprise $>99.8\%$ gaseous Na, SiO, Fe, K, and Mg. The major constituents are Na and SiO at high temperatures, whereas the mixing ratio of SiO rapidly decreases below 2400 K (Figure 2). The partial pressure of Mg behaves similarly to SiO but does not exceed 1% of the atmospheric mixing ratio for any composition. The mixing ratios of Fe and K, however, are more variable because they depend on the assumed magma ocean composition and reach their highest mixing ratios of 9% and 2%, respectively, for CB and EH4 compositions with high FeO and K_2O (Table 2, Figure 2). Refractory components—AlO and Ca—have negligible partial pressures ($<10^{-6}$ bar at 2400 K) and are thus ignored in further calculations. The highest total surface pressure of metal-bearing species at low temperatures is obtained with the NSP melt composition. At 2400 K, the total surface pressure is 6.16×10^{-2} bar, which decreases to 8.52×10^{-6} bar at 1500 K.

Figure 3 shows the homopause levels of Na for the nonvolatile cases as a function of time for CB and NSP melt compositions. Exobase levels lie within a few hundreds of kilometers of the homopause and are omitted in the log–log plot as a result. During the magma ocean phase, the levels evolve within 470–660 yr for N5 cases and 1100–1480 yr for N3 cases. The homopause and exobase locations are only weakly sensitive to the planet size and gravity. The magma ocean composition, however, exerts a strong influence on the atmospheric structure. For the CB case, the homopause lies at 685 km, whereas for the NSP melt composition it lies at around 1258 km at a magma ocean surface temperature of 2400 K. The early inflation of an atmosphere above a cooling magma ocean is due to increasing $T_{\rm skin}$ caused by decreasing IR opacity as the partial pressure of SiO decreases (Equation (7)). Following this stage, the homopause altitude falls to 83 km (CB) and 439 km (NSP melt) at 1500 K. The exobase density and location are further dependent on the mean cross section of atmospheric species, which is tied to the composition-dependent vapor pressures (Equation (6)). The high vapor pressure of Na in the NSP melt relative to the CB composition lowers the mean molecular weight and the mean CCS of the atmosphere, which both increase its extent.

3.1.2. Volatile Cases

Volatile-bearing cases result in cooling times of 3400 yr (Case SV) and 8900 yr (Case LV). Both small proto-Mercury and large proto-Mercury have the same initial volatile abundances of C and H by ppmw, but this manifests in a larger total reservoir size of volatiles for a large proto-Mercury compared to a small one. The mass of volatiles in the atmosphere defines the surface atmospheric pressure, which in turn determines the optical thickness of the atmosphere and hence the efficiency of radiative cooling.

Atmospheres of volatile cases around a small and large proto-Mercury reach surface pressures of about 5 and 12 bar at a magma ocean surface temperature $T_{\rm surf}$ of 2000 K, respectively (Figure 4). This result is independent of the partial pressures of the metal-bearing species, as their contribution is $\leqslant 0.1$ bar at $T_{\rm surf} = 2000$ K. Thus, it is the outgassed hydrogen and carbon species (which depends on their solubilities) that dictates the surface pressure. VULCAN is then used to compute the equilibrium chemistry of the atmosphere accounting for the outgassed volatiles, as well as the metals and oxides. For both small and large Mercury, the atmosphere below the homopause is dominated by H_2 and CO with about 60 and 27 vol.%, respectively, at $T_{\rm surf} = 2000$ K. Between the homopause and the exobase the dominant H-, C-, and O-based species dissociate to monoatomic gases.

For all compositions, Na and K are the dominant metallic elements at $T_{\rm surf} = 2000$ K. At the surface their hydroxide forms NaOH and KOH are fairly abundant, but they dissociate toward the homopause (Table 4). Sodium hydride (NaH) is also present at the surface at pressures one order of magnitude lower than NaOH and remains about constant throughout the atmosphere, reaching similar mixing ratios to K. Potassium hydride (KH) is ignored, as no rate constant exists in the NIST kinetics database (kinetics.nist.gov).

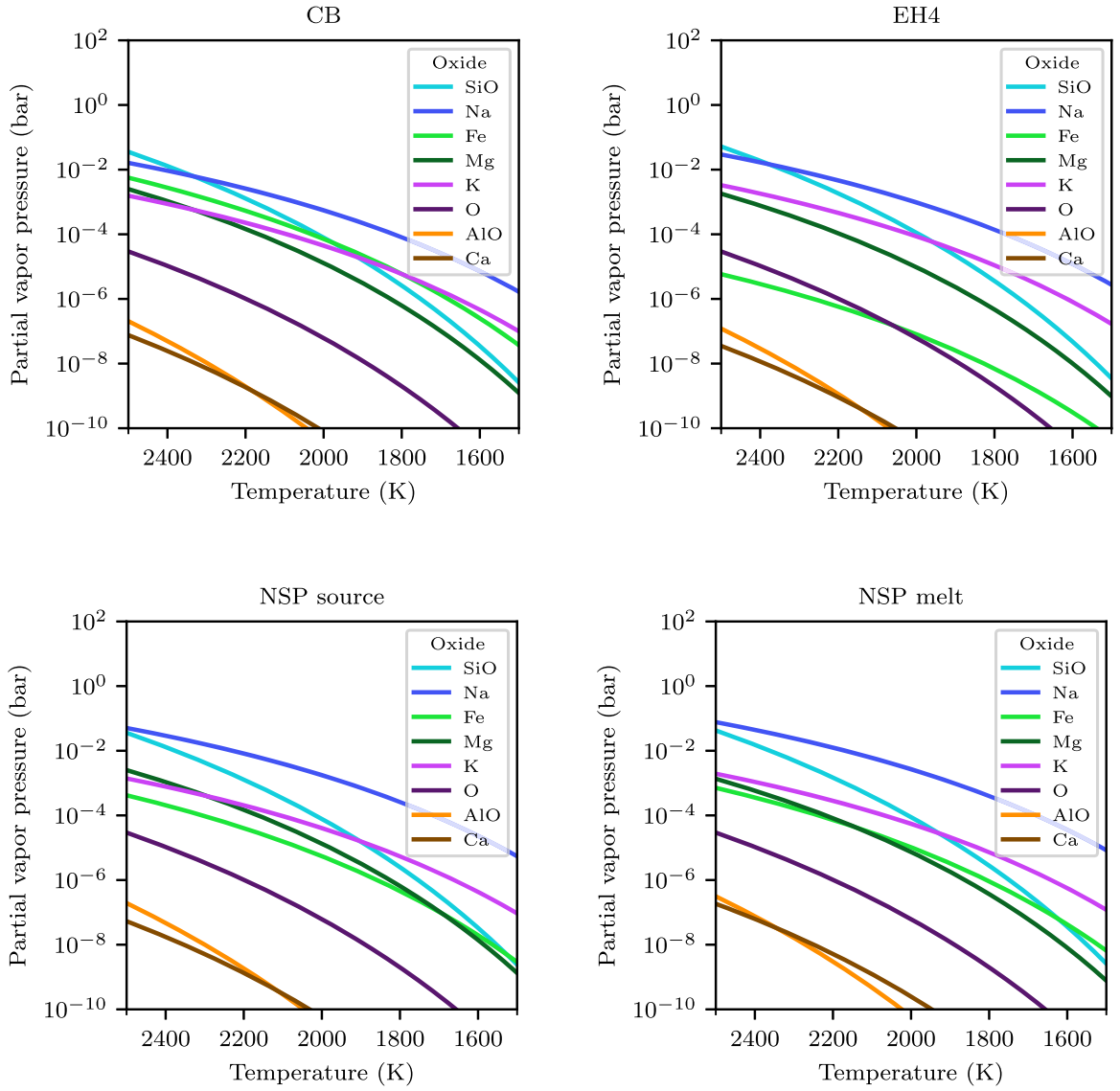

Figure 2. Oxide partial vapor pressures calculated using the CB, EH4, and NSP source and NSP melt composition. The mixing ratios are thereby reflected by the activities of the elements in the given melt composition. The high-Fe composition CB shows a large Fe partial pressure, comparable with K in the high-K compositions EH4 and NSP melt.

Exobase levels are situated up to 2910 and 2590 km for small and large Mercury with homopause levels down to 2360 and 2160 km, respectively. The *P*–*T* structure of the atmosphere gives $T_{\rm skin}$ values for the homopause and exobase of about 1021 and 893 K (Table 4), respectively, for small and large cases, which lies well below the $T_{\rm skin}$ calculated for the nonvolatile cases ($T_{\rm skin} = 1615$ K). The exobase levels of the volatile cases are thus comparable to the nonvolatile cases. Unlike the nonvolatile cases, the planet size has a large impact on the atmospheric structure, which is solely due to the difference in the total volatile reservoir (Section 3.1).

3.2. Atmospheric Loss

We find that the major atmospheric escape mechanism is photoevaporation (Equation (10)), with a lower limit of photoevaporation constrained to $10^{6.6}$ kg s^{-1} and an upper limit of $10^{9.6}$ kg^{-1} for both nonvolatile (Na) and volatile cases (H, C, and O). The upper limit is thereby roughly three orders of magnitude larger than the photoionization of the major atmospheric species. For the high heating efficiency ($\eta_{\rm EUV} = 10^{-1}$) case, loss rates become evaporation limited when reaching 1600 K as the surface-to-equilibrium pressure ratio approaches zero. For low heating efficiencies ($\eta_{\rm EUV} = 10^{-3}$), the ratio of surface to equilibrium pressure $p_{i,s}/p_{i,\rm eq}$ remains at >0.93 (Equation (12)). Photoevaporation as an approximation of thermally driven hydrodynamic escape (Equation (10)) therefore expresses the highest uncertainty on the stability of the atmosphere.

Figure 5 shows the integrated mass loss over the most extensive surficial melt lifetime of 8900 yr. The photoevaporative erosion *dR* of the surface can be estimated by assuming mass conservation where

$$\frac{dM}{dR} = 4\pi R_P^2 \rho_{\rm mantle}. \quad (13)$$

Using a mantle density of $\rho_{\rm mantle} = 3.5$ g cm^{-3} and assuming a high EUV heating efficiency of 10^{-1} at a large Mercury size allows for ~2.3 km loss of crust over the 8900 yr of the volatile case surficial melt lifetime. We have shown using Equation (12)

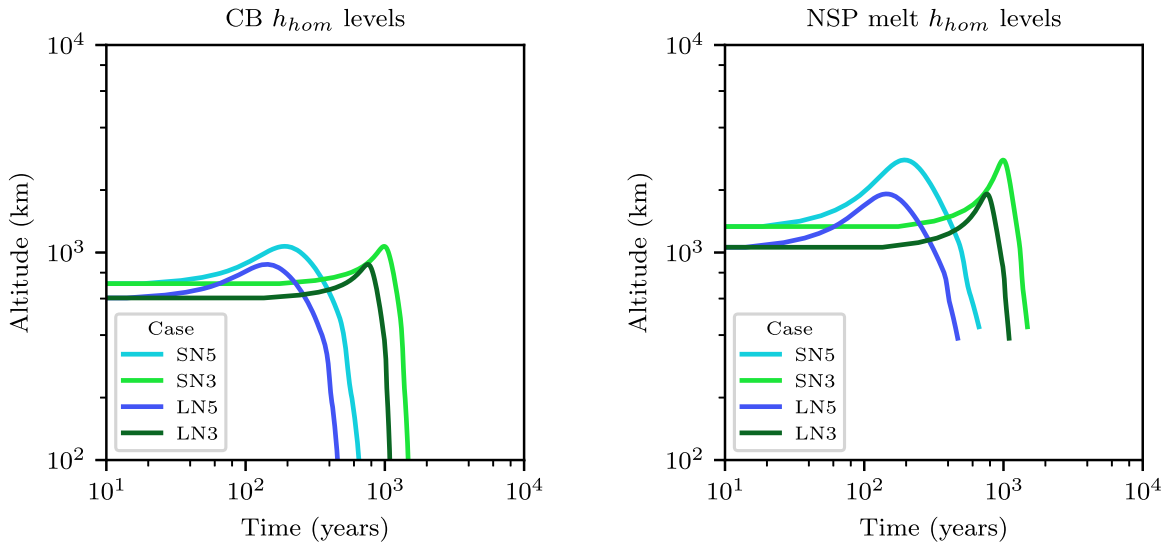

Figure 3. Homopause altitudes for sodium derived for the nonvolatile cooling scenarios for CB and NSP melt. Lines terminate when the surface temperature reaches 1500 K. The equilibrium exobase levels are not plotted, as they lie close to the homopause levels. Homopause levels for other species show the same trends and reach comparable elevations.

that this case becomes evaporation limited owing to the high photoevaporation rates. The total integrated loss when assuming an EUV heating efficiency of 10^{-1} is therefore lower than shown in Figure 5 but not significantly. This is due to most loss occurring during the early magma ocean stage, when the surface temperatures are high and evaporation is not limiting the potentially high photoevaporation rates.

Plasma-driven escape is diffusion limited, as a supply is required at the exobase (Equation (5)). The $\dot{M}_P$ calculated lie orders of magnitude below $\dot{M}_{\rm ion}$ as given in (Table 5) and therefore do not affect the atmospheric structure. Using an intermediate total pressure of 25 nPa, we find about $\dot{M}_P = 10^{3.4}$ kg s^{-1} for small and large, nonvolatile Mercury cases and about $\dot{M}_P = 10^{3.1}$ kg s^{-1} for volatile Mercury cases, respectively. The loss rates are thereby comparable to the plasma-driven escape observed on Jupiter's moon Io in SO_2 $\sim 10^3$ kg s^{-1} (Thomas et al. 2004).

Time-averaged mass-loss rates by photoionization are given in Table 5. Like nonthermal plasma-driven escape, nonthermal escape due to photoionization at the exobase (Equation (9)) is diffusion limited. As photoionization rates of nonvolatile cases follow the same trends independent of planet size, we report results focusing on a small proto-Mercury only, omitting the large Mercury photoionization rates, which are mostly within a factor of two for the dominant species (Table 5). The results of nonvolatile N5 cases are also not reported, as an almost isothermal atmosphere results in less than a factor of two larger loss rates at high temperatures.

Regarding the presence of metal-oxide-derived gaseous species, Gibbs free energy minimization of the vapor phase (using FactSage) along a case-dependent atmospheric P–T profile (Figure E1, Appendix E) indicates that Mg and SiO condense into clinopyroxene (1900 K) and then into olivine ($\approx$1700 K) during cooling, by which temperature their fraction remaining in the gas is negligible. Iron persists in the vapor to lower temperatures, condensing partially into olivine before iron metal condenses at 1350 K. Therefore, while Mg and Si (and Ca and Al) all condense prior to reaching the exobase ($T \approx 1680$ K), Fe is likely to partially reside in the vapor phase. Sodium never fully condenses (nepheline, its major host mineral, condenses in very minor proportions below 1500 K), while K remains entirely in the vapor phase down to at least 950 K.

3.2.1. Loss from Nonvolatile Atmospheres

$\dot{M}_{\rm ion}$ in nonvolatile cases is sensitive to the chosen initial composition (Figure 6). The loss fluxes of the nonvolatile species of interest—SiO, Na, and K—are proportional to their mixing ratios in the atmosphere (Figure 2). In cases with high initial SiO partial pressures the mixing ratios and hence the diffusion-limited loss rates of Na and K increase during initial cooling as SiO becomes less abundant. This is most evident in the CB loss flux with an initially increasing loss rate despite decreasing temperatures (Figure 6).

In the low-Na and low-K composition CB, where SiO is the dominant metal oxide at high temperatures, loss fluxes of SiO reach up to 9.6×10^5 kg s^{-1} at $T_{\rm surface} = 2400$ K. The vapor pressure of SiO declines with respect to other dominant gas species (Na and K), thereby reducing its mixing ratio rapidly with decreasing temperature. The lower mixing ratio of SiO causes loss rates to drop to 9.4×10^2 kg s^{-1} at 1500 K. For the same composition, loss rates for Na and K are around 2.0×10^5 kg s^{-1} and 3.1×10^3 kg s^{-1} at $T_{\rm surf} = 2400$ K, increasing to 3.2×10^5 kg s^{-1} and 4.2×10^3 kg s^{-1} at $T_{\rm surf} = 1500$ K, respectively. For the high-Na end-member composition of NSP melt, the diffusion-limited loss rates for Na and K are 5.9×10^5 kg s^{-1} and 1.2×10^4 kg s^{-1}, respectively, when at $T_{\rm surf} = 2400$ K and decrease to 3.9×10^5 kg s^{-1} and 4.3×10^3 kg s^{-1}, respectively, when $T_{\rm surf} = 1500$ K. The ratio of Na to K diffusion rates is $\sim$100 and hence about one order of magnitude higher than their mixing ratios in the atmosphere. Integrated diffusion-limited losses over the surficial melt lifetimes are shown in Figure 7.

If we assume, based on FactSage results, that SiO and Mg are absent and only Na, K, and Fe remain in the atmosphere, the diffusion-limited loss rates for all cases peak in the small Mercury NSPm case with a fairly temperature-independent Na loss rate of about 10^6 kg s^{-1}. Loss rates for K and Fe are thereby about three orders of magnitude lower than that of Na and do not significantly contribute to the total loss. The difference in change

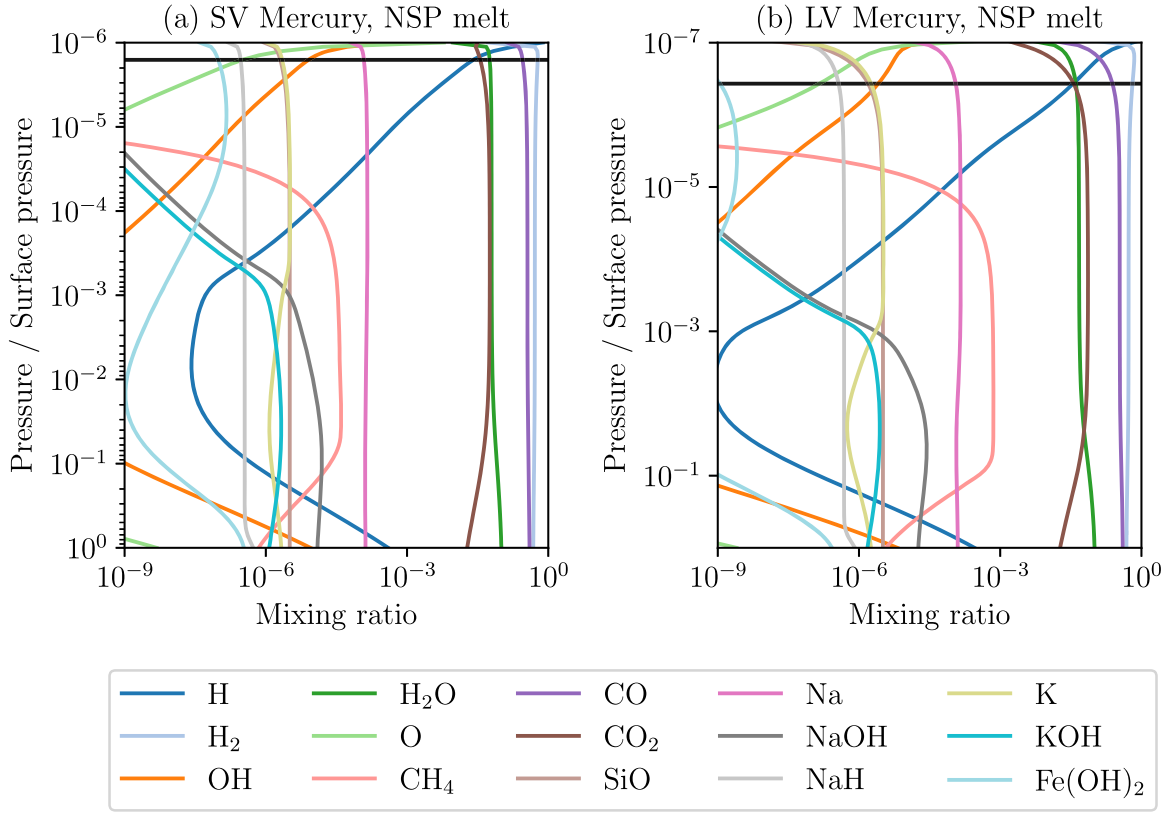

Figure 4. Major- and minor-element composition of the atmosphere for NSP melt composition with a surface temperature of 2000 K for (a) SV and (b) LV Mercury models. The surface pressure that normalizes the *y*-axis is 5.0 bar for SV and 12.1 bar for LV. The homopause level of H is plotted as a black horizontal line.

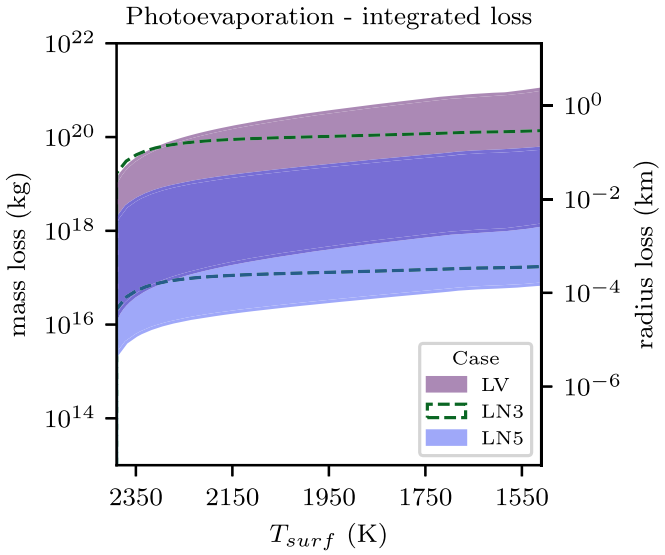

Figure 5. Integrated mass-loss rates of the bulk atmosphere through photoevaporation from 2400 to 1500 K for large Mercury cases. The shaded areas represent the uncertainty of loss rates based on initial conditions. For the N3 case only the upper and lower limits are shown as dashed lines, as it lies within both V and N5 areas. The highest loss rates assume upper limits for EUV luminosity only 1 Ma after Sun formation, $L_{\rm EUV}$(1 Ma), and heating efficiency of 10^{-1}, and the lowest assume $L_{\rm EUV}$(5 Ma) and heating efficiency of 10^{-3}. Using a mantle density of $\rho_{\rm mantle}$= 3.5 g cm^{-3} results in a maximum of crust material being lost to space ranging between 2.3 km and 16 cm, depending on the degree of XUV intensity and heating efficiency.

Table 5
Time-averaged Mass-loss Rates in kg s^{-1}

Mass Loss (log10)			
Process	Size	Emissivity	
		N5, N3	V
$\dot{M}_P$	S	3.4	3.1
	L	3.4	3.2
$\dot{M}_{\rm ion}$ ($\dot{M}_{{\rm diff},i}$)	S	5.6	5.6
	L	5.2	5.8
$\dot{M}_U$		$L_{\rm EUV}$	
		t = 1 Myr	t = 5 Myr
$\eta_{\rm EUV}(10^{-3})$	S	7.5	6.6
	L	7.6	6.7
$\eta_{\rm EUV}(10^{-1})$	S	9.5	8.6
	L	9.6	8.7

Note. Loss rates of plasma heating $\dot{M}_P$, photoionization $\dot{M}_{\rm ion}$, and photoevaporation $\dot{M}_U$. Photoevaporation is insensitive to the atmosphere's emissivity and composition but depends on the EUV flux and the EUV heating efficiency (end-members of 10^{-3} and 10^{-1}). The EUV flux is a function of the age of the solar system (Equation (8), after Johnstone et al. 2015; Tu et al. 2015).

of $\dot{M}_{\rm diff}$ and thus $\dot{M}_{\rm ion}$ between species with continued magma ocean cooling results from the constantly dropping total surface pressure simultaneously to shifting partial pressures. At low magma ocean surface temperatures, Na exerts most of the pressure, whereas at high temperatures condensing species, such as SiO, are the predominant contributors to the total pressure and mean molecular mass of the atmosphere (Figure 2). A lower surface pressure results in a lower homopause level and leads to

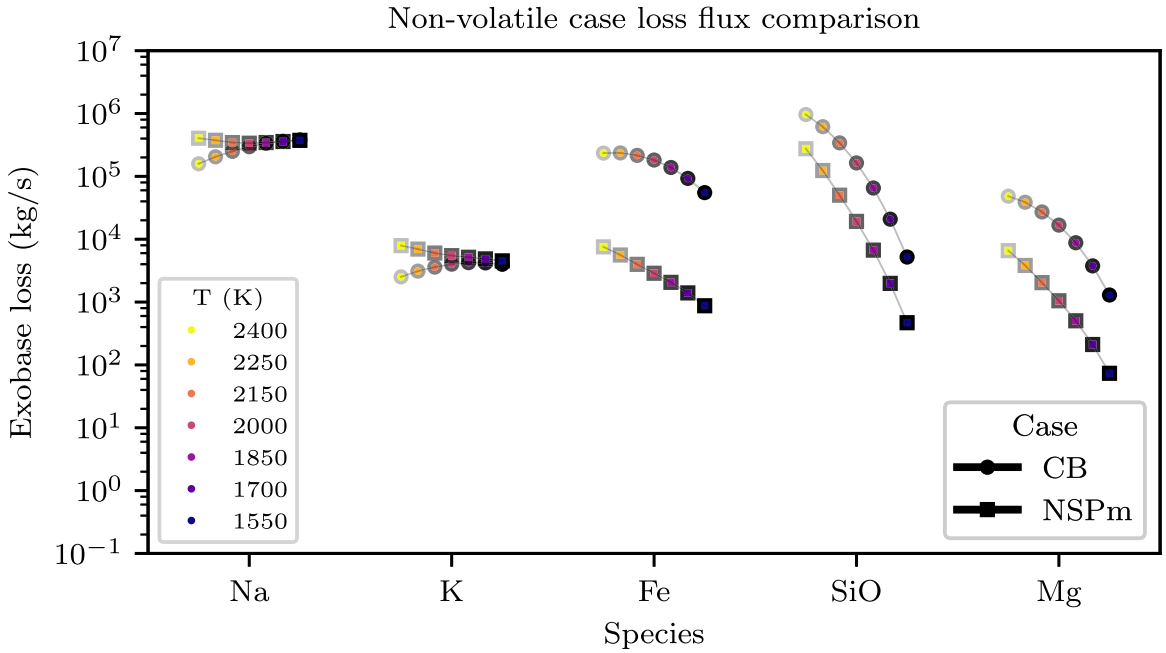

Figure 6. Mass-loss fluxes of exospheric species from 2400 to 1550 K plotted for the small Mercury N3 cases. The loss fluxes for large Mercury follow the same trends and are about a factor of two smaller. The N5 cases with isothermal atmospheres show a factor of two larger loss rates at high temperatures but the same species-related trends.

a smaller diffusion area and rate; however, the rapid decline of the SiO partial pressure in the atmosphere (n_{SiO}/n_{hom}) results in the sharp drop of SiO homopause diffusion rates (i.e., Equation 5) but increases the T_{skin} and therefore the extent of the atmosphere (Figure 3). Similarly, the loss rates through ionization at the exobase for a relatively low mean molecular weight ("light") Na-, K-, and Fe-based atmosphere are up to a factor of five higher than the 2×10^5 kg s^{-1} loss of Na from a "heavy" atmosphere, which includes Mg and notably SiO.

These limits are significant for atmospheric escape estimates by plasma heating, photoionization, or Jeans escape. All three of those processes are calculated from the exobase, which is for plasma heating and photoionization where ions and photons can access a rarefied neutral atmosphere. This is therefore diffusion limited, as a high flux is required to source the neutral species experiencing a momentum transfer from the plasma. Photoevaporation is not necessarily diffusion limited so long as a sufficiently large column exists at the altitude where EUV photons are able to absorb onto infrared-emitting molecules (z_{abs}, Figure 8). In N_2/CH_4 atmospheres (e.g., Kuiper Belt objects) the critical column density is estimated to be $\gtrsim 10^{18}$ cm^{-2} (Johnson et al. 2015), which is easily achieved at a fiducial absorption altitude of z_{abs} situated at $\sim$1.25 R_P, where the column density is equivalent to $\sim 10^{21}$ cm^{-2} for an isothermal scale height of $H \approx 150$ km at a $T_{surf} = 2000$ K. For a magma–silicate atmosphere, as studied here, SiO or a similar species would be able to reemit in the infrared, resulting in upper atmospheric expansion and Roche lobe overflow to space.

3.2.2. Loss from Volatile Atmospheres

In the volatile cases, assuming a speciation as encountered at the H homopause, the diffusion-limited loss fluxes of primary species lie between 10^4 and 10^5 kg s^{-1} for all major species (H_2, CO, H_2O, and CO_2) in the small and large proto-Mercury cases.

The loss fluxes of minor species Na and K are several orders of magnitude lower than those of the major species, at 10^1 and 10^0 kg s^{-1}, respectively. In the nonvolatile cases, loss fluxes of Na and K are directly proportional to their thermodynamic activities in the melt. Sodium activity increases by about a factor of 4.5 from the CB to NSP melt composition and K by a factor of two between NSP source and EH4, respectively. Relative to nonvolatile cases, loss fluxes for Na and K are several orders of magnitude lower in the high-pressure, volatile-rich atmosphere at $T_{surf} = 2000$ K.

If we assume the loss fluxes of the dominant H-, C-, and O-based species at $T_{surf} = 2000$ K to be constant over the lifetime of the molten surface (Section 3.1) and integrate them for small and large Mercury volatile cases, we obtain a total mass loss by photoionization of 4.1×10^{16} kg and 1.8×10^{17} kg, respectively. This exceeds the total photoionization mass loss from the low absorbing N5 nonvolatile case by only about one order of magnitude (Figure 7). The mass loss of Na in the volatile cases, however, only contributes about 10^{12} kg of the total, which is about four orders of magnitude below the total mass loss of the nonvolatile cases. Again, this assumes that the Na loss flux is constant in the volatile case. This is deemed appropriate because Na is only a minor component of such atmospheres, is lost at slow rates that represent an insignificant fraction of its total budget, and does not condense before reaching $T_{surf} = 1500$ K.

4. Discussion

4.1. Mass Loss of Proto-Mercury

Table 5 tabulates the total atmospheric loss rates due to the following escape mechanisms: ionization $\dot{M}_{ion}$, photoevaporation $\dot{M}_U$, and plasma heating $\dot{M}_P$. Figure 8 illustrates the atmospheric level from where the degassed magma ocean atmosphere is escaping.

We find that the loss fluxes from the exobase caused by photoionization and atmospheric sputtering are supply limited

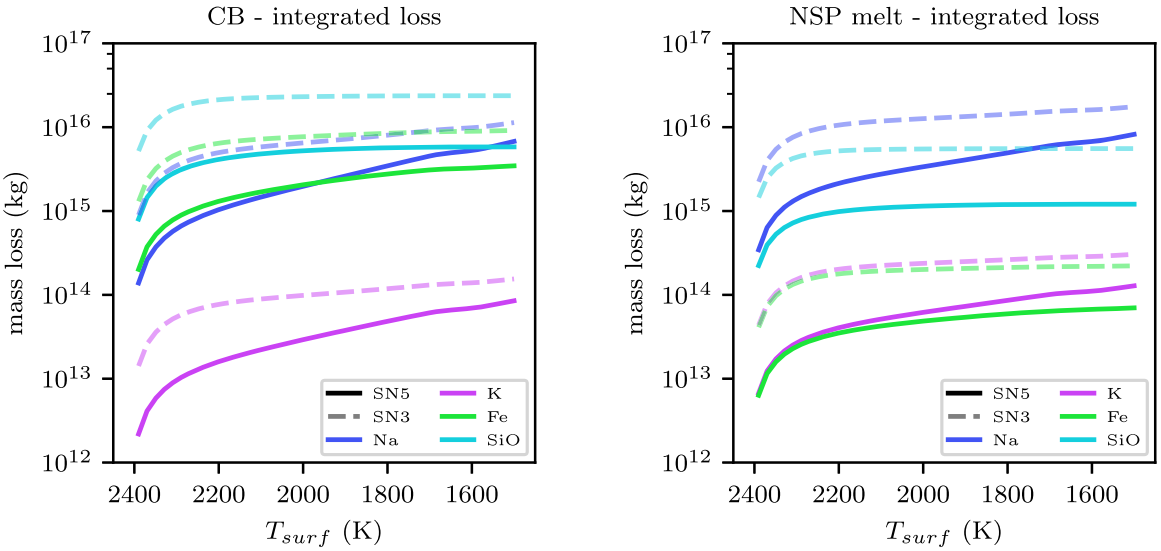

Figure 7. Integrated mass-loss rates of exospheric oxides and elements through photoionization as the magma ocean cools from a surface temperature of 2400 to 1500 K. SiO loss is shown, although it is unlikely to persist in the upper atmosphere, as it is consistently below its highest condensation temperature of $T = 1900$ K.

(in all volatile and nonvolatile cases) by homopause diffusion $\dot{M}_{\rm diff}$, which dictates the exobase elevation in order to remain in steady state. The maximum $\dot{M}_{\rm ion}$ of volatile and nonvolatile cases are comparable, even though their atmospheres are composed of different major species (nonvolatile case: Na and SiO; volatile case: H_2, H_2O, CO, and CO_2). This similarity is attributed to the higher $T_{\rm skin}$ of the nonvolatile cases at $T_{\rm surf} = 2000$ K, caused by IR opacity, which is tied to the mixing ratio of SiO. SiO pressure rapidly decreases with decreasing temperatures, which is contrary to CO_2 and H_2O in the volatile cases. A higher skin temperature in the nonvolatile cases hence compensates for the lower atmospheric pressures.

The photoevaporation rate is limited by the degree of upper atmospheric heating efficiency, $\eta_{\rm EUV}$, rather than by $\dot{M}_{\rm diff}$, as well as by the supply of gases from surface evaporation (Equation (12)). The assumption of a constant photoevaporation rate is thus only valid for evaporation at high temperatures above 1600 K, at which evaporation rates are fast enough for supply to be sustained, or for moderate mass-loss rates of about 10^7 kg s^{-1}. The majority of mass loss occurs at high temperatures (Figure 5) when surface evaporation rates are high compared to photoevaporative loss rates, the latter of which are independent of temperature and depend instead on the EUV flux.

The diffusion-limited loss rates by photoionization of the four major volatile species, H_2, H_2O, CO, and CO_2, from a volatile-rich atmosphere total $\sim 10^5$ kg s^{-1}. The loss of Na from a thick, volatile-rich atmosphere is inhibited by its low mixing ratios at the homopause and exobase. Therefore, diffusion-limited loss of Na is most efficient when the atmosphere is thin, reaching a few $\times 10^5$ kg s^{-1}, which coincides with the total mass-loss rates from volatile cases. The total integrated mass loss by photoionization from Mercury's exosphere is low for small volatile and nonvolatile cases with $\leqslant 4.1 \times 10^{16}$ kg and $\leqslant 3.0 \times 10^{16}$ kg, respectively.

The mass loss of single species is negligible compared to the total inventory of the magma ocean reservoir. For example, 0.033 wt% H_2O and a low estimate of 0.1 wt% Na in a total mass of $M_{\rm MO} \approx \times 10^{23}$ kg correspond to a reduction of the total H_2O reservoir mass (volatile cases) and Na (nonvolatile cases) by $\leqslant 0.02\%$. Assuming a well-mixed mantle reservoir, the bulk composition of Mercury would not significantly change even for species with low abundance in the reservoir and large loss rates such as H_2O, CO_2, and Na. Energy-limited escape via photoevaporation, however, can erode up to 2.3 km of Mercury's crust, which is equivalent in mass to 0.3% of small Mercury (Figure 5). Assuming small heating efficiencies, as well as a lower EUV flux, leads to integrated photoevaporation losses and eroded crust thicknesses that are reduced by four orders of magnitude.

Physical segregation between crystal and liquid during magma ocean cooling will induce chemical fractionation of element abundances with respect to those of the bulk mantle. Namely, the incompatible lithophile elements (Na, K, Al, and Ca) become enriched in late-stage liquids of a Hermean magma ocean. This effect is simulated by considering the composition of the NSP melt as a surface magma ocean analog relative to that of its inferred source. These differences notwithstanding, the partial pressures of metal-bearing gas species vary only marginally among EH4, CB, and NSP compositions. This is due to two factors: (1) vapor pressures of different elements vary by orders of magnitude among one another (e.g., compare Na with AlO), whereas abundances of these major elements vary only by a factor of 2–3 in most cases; and (2) higher mole fractions of Na and K in the NSP melt are partially compensated by their lower activity coefficients relative to the NSP source or EH4 composition. As we show in Section 3, all elements other than Na and K, and potentially Fe, condense before reaching the exobase. We can therefore conclude that the atmospheric pressure and speciation around proto-Mercury only depend on the abundance of volatile and moderately volatile elements.

4.1.1. Early Origin of Surface Na

In order to determine the potential impact of a magma-ocean-generated atmosphere on the surface composition of a small proto-Mercury, we calculate the total mass of Na in the atmosphere. We consider a hypothetical scenario in which the atmosphere collapses as soon as the first crust forms, coinciding with the termination of the magma ocean stage when a surface temperature of 1500 K is reached. To obtain a

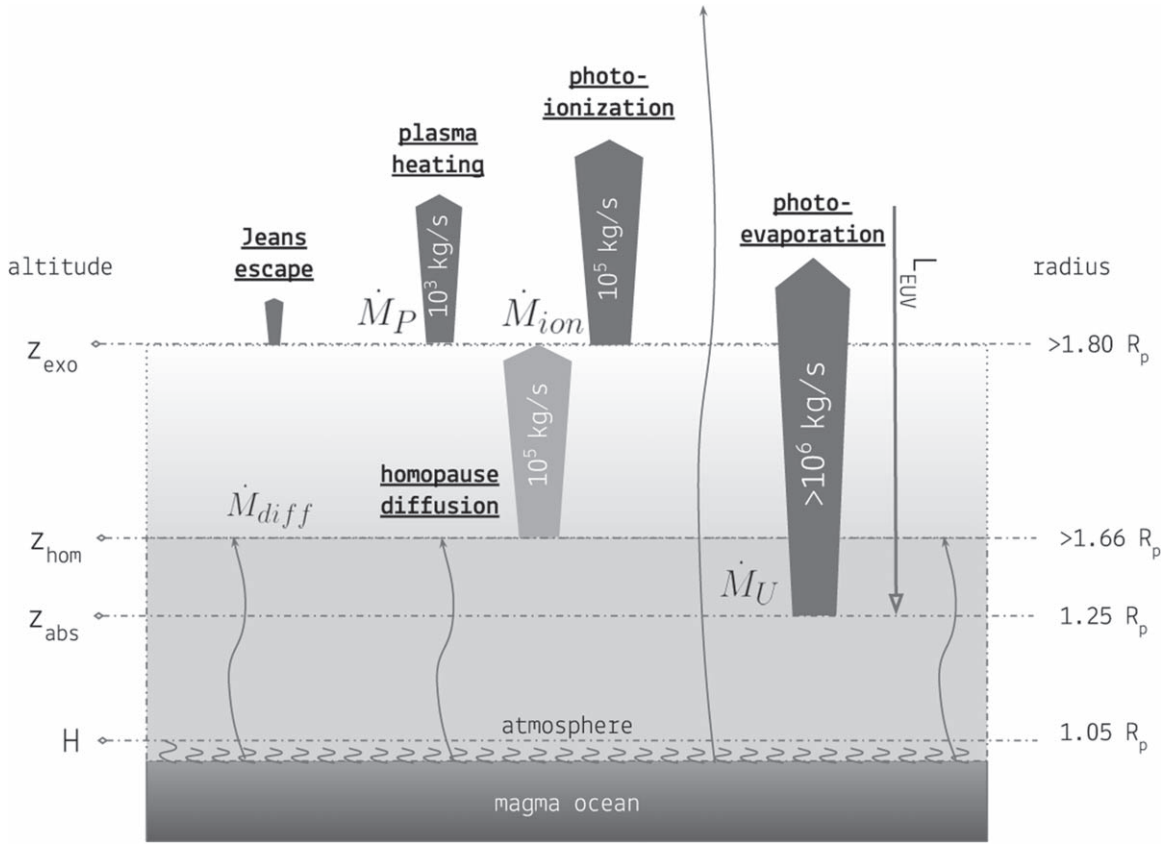

Figure 8. Mass-loss processes and their rates demonstrate the coupling between various atmospheric layers. R_P is the planet radius, z_{exo} is the exobase altitude, and z_{hom} is the homopause altitude that governs exospheric loss processes of Jeans escape, plasma heating $\dot{M}_P$, and photoionization $\dot{M}_{ion}$. z_{abs} is the absorption altitude where upper atmospheric heating (photoevaporation) $\dot{M}_U$ commences. The absorption altitude is assumed to lie below the homopause, and therefore photoevaporation is not limited by homopause diffusion.

result that is consistent with the notion of Na-poor building blocks (e.g., Humayun & Cassen 2000), we use the low-Na CB composition (Table 2) and its H- and C-absent pure Na atmosphere composition. The resulting total amount of Na integrated over the whole atmosphere yields about 10^{11} kg.

Whether it precipitates as Na metal or as another compound depends on the composition of the atmosphere that exists. Although not considered in our model, such an atmosphere would contain significant quantities of other moderately volatile elements that could combine with Na to form complex molecules, namely, F, Cl, and S. The species NaCl is inferred to be stable among volcanic gases (e.g., Aiuppa et al. 2003) and has been directly observed in Io's atmosphere (Lellouch et al. 2003; Moullet et al. 2010), and it may therefore be a potential candidate to form surficial deposits. Sodium chloride is also observed as a stable precipitate from experimentally generated volcanic gas analogs (Renggli & Klemme 2020) and is therefore likely to occur as an Na-bearing phase on the Mercurian surface. This is supported by the coinciding distribution pattern of Na and Cl from more recent volcanic deposits found in gamma-ray spectrometer data (Evans et al. 2015).

Here we consider a simplified case, for which the mass of sodium in the atmosphere is uniformly distributed over the surface of Mercury as pure, low-density, Na metal, resulting in a layer less than 1 mm for the CB case. Using a more Na-rich composition like EH4, combined with an increased atmospheric reservoir size of large proto-Mercury, would lead to a factor of four thicker Na layer, but still less than 1 mm. In the volatile cases (i.e., with CO_2 and H_2O), the amount of Na in the atmosphere is identical to the volatile-free cases, as, in our model, the partial pressure of Na is independent of the presence of volatiles. The small dissolved quantities of CO_2 and H_2O in the silicate melt ($\leqslant$1000 ppm) should thereby not influence the activity coefficients of the major rock-forming species. This hypothetical Na metal layer would not outlast meteorite impacts, which are assumed to have removed 50 m to 10 km of early crust (Hyodo et al. 2021). For the enrichment to be preserved, the atmospheric sodium would have to be incorporated into a layer with a thickness exceeding the removed crust. However, for a minimum layer of 50 m we obtain a total Na wt% increase of merely $\sim$1 ppm and $\sim$10 ppb for small and large proto-Mercury cases, respectively. We thus conclude that the collapse of an early Na-rich atmosphere would not contribute to a notable increase of Na in the surface.

4.2. Controls on Mass Loss

The mean column density at the exobase depends on the weighted average of the dominant species' CCSs. Loss rates are directly related to the exobase density. However, using CCSs from Kim & Desclaux (2002) that are about one order of magnitude smaller would reduce the homopause and exobase levels by a few tens of kilometers and decrease the homopause diffusion-limited loss by $\leqslant$2%. The sensitivity of mass loss to the chosen CCSs is therefore weak. In nonvolatile cases, if we consider that all species except Na, K, and Fe condense (FactSage in Section 3), then mean molecular mass and the CCS of the atmosphere decrease, which enhances molecular diffusion

(Equation (4)). This pushes the homopause and therefore the exobase farther from the planet surface, increasing the atmospheric surface area and therefore loss. Furthermore, the absence of SiO leads to a hotter skin temperature as the atmosphere becomes IR transparent, further enhancing loss. The difference of the ionization mass-loss rate at the exobase between an Na, K, and Fe atmosphere and an atmosphere where SiO is a major component at high temperature is thereby about a factor of three larger for all cases.

For rocky exoplanets on short orbits, the atmospheric temperature around our homopause levels (10^{-7} bars) can be as high as 3800 K for a surface temperature of 2400 K (Ito et al. 2015). Mercury possesses different planet parameters (1 $M_{\rm Earth}$ and 0.02 au vs. 0.055 $M_{\rm Earth}$ and 0.3 au for Mercury); however, the more intense early UV flux experienced by Mercury could similarly boost the temperature at the homopause. Calculations with an increased skin temperature of 3800 K at the homopause resulted in about a factor of two higher photoionization loss rates for all cases.

We used photoevaporation as a proxy for thermally driven hydrodynamic escape. Krenn et al. (2021) have shown for a large range of parameters that photoevaporation can underestimate hydrodynamic escape especially at low EUV fluxes. Given our large incident EUV fluxes of about 10^2–10^3 $\mathrm{Js^{-1}\ m^{-2}}$ and our escape parameters (Table 4), we expect to be within one order of magnitude of thermally driven hydrodynamic escape rates (compare EUV fluxes and escape parameters to Figure 4 in Krenn et al. 2021, although our escape parameters for small Mercury lie just below the shown range).

4.3. Atmospheric Evolution and Structure

Figure 8 illustrates the transport of mass away from different levels in the atmosphere. In our model, atmospheric escape can be either energy limited (e.g., $\dot{M}_U$) or diffusion limited (Jeans escape, $\dot{M}_P$, $\dot{M}_{\rm ion}$). Below we describe the role of enhanced atmospheric heating or cooling on diffusion- and energy-limited escape.

Diffusion rates are tied to the homopause density, which determines the homopause altitude. The eddy diffusion coefficient (K_{zz}) needed to determine $n_{\rm hom}$ bears large uncertainties, however. For all cases, a K_{zz} larger than the Earth-derived upper limit of 3.2×10^6 $\mathrm{cm^2\ s^{-1}}$ would most likely be adequate to accommodate proto-Mercury's increased atmospheric temperature, increasing $z_{\rm hom}$ and lowering $n_{\rm hom}$, leading to a slightly larger diffusion and therefore loss rate. Even if we assume a larger K_{zz}, however, homopause diffusion will remain the limiting factor for mass loss. We find for volatile cases that even if K_{zz} is three orders of magnitude larger, the total loss for volatile cases increases by a factor of less than two. The sensitivity of $\dot{M}_{\rm diff}$ and therefore $\dot{M}_{\rm ion}$ to the eddy diffusion coefficient is therefore weak.

Ionization could further increase the exobase temperature, and hence the reported diffusion-limited loss fluxes could be a lower limit. Whether mass loss occurs from the exobase surface, or whether it is the result of an advective outflow, is canonically assessed by the escape parameter (e.g., Genda & Abe 2003). If the escape parameter $\lambda_0 \leqslant 3$, the atmosphere experiences mass outflow owing to its nonzero net velocity, and escape occurs inward of the exobase at the sonic point (where the thermal velocity exceeds the sound speed). If $\lambda_0 \gg 3$, the atmosphere escapes because the mean free path is longer than the scale height, and Jeans escape prevails. Table 4 shows how the exospheric escape parameters are all $4 \leqslant \lambda_0 \leqslant 15$, a near-transitional escape regime between Jeans- and hydrodynamic end-members, which was recently determined to be relevant for the putative magma ocean on the Moon (Tucker et al. 2021). These authors demonstrated via direct simulation Monte Carlo simulations (Bird 1994) that cooling due to escape is important for $\lambda_0 \lesssim 15$. Therefore, in Table 4, based on our escape parameters, it would appear that although ionization may further enhance escape, cooling may temper this loss. In addition, the significant ionization rates of $\dot{M}_{\rm ion} \simeq 10^6$ $\mathrm{kg\ s^{-1}}$ at the semimajor axis of proto-Mercury promote the generation of an ionosphere that is modulated by the planetary magnetic field. Simulations on an early Mars analog have demonstrated that ion escape is efficient at removing material (Egan et al. 2019). Therefore, it is possible that we are underestimating escape by not considering magnetic interactions.

In the concurrent "energy-limited" regime it would appear that if EUV photons are able to absorb onto a sufficiently high flux of molecules (Section 3.2.1), heating would overwhelm cooling. However, based on the escape parameters in Table 4, it appears that cooling associated with escape may be important, arresting loss. At the same time, the study of low-mass, close-in exoplanets orbiting Sun-like stars has posited the idea that low-mass planets are nevertheless born with hydrogen/helium (H/He) envelopes, although these are rapidly lost owing to photoevaporation (Mordasini 2020). For an H/He envelope equivalent to 1% the mass of proto-Mercury, we find that our upper limit on photoevaporation results in the dissipation of an H/He envelope in $10^{4.4}$ yr, which is larger than the lifetime of the molten surface. The possibility of an H/He envelope to persist during the molten surface lifetime is therefore nontrivial and could result in significant heating, which could not only enhance escape but also elongate the melt lifetime past the 10^4 yr we study here.

4.4. Origin and Evolution of Mercury

The elevated core:mantle ratio, coupled with an Na- and S-rich surface, distinguishes Mercury from the other terrestrial planets. Two key hypotheses exist to account for these characteristics: (1) the preferential loss of silicate material, either by evaporation (Fegley & Cameron 1987) or by collisional stripping (Benz et al. 1988), and (2) equilibrium condensation and sorting of metal from silicate in the solar nebula (Lewis 1972; Weidenschilling 1978).

In evaluating hypothesis (1), Fegley & Cameron (1987) concluded that ∼75%–79% of silicate material would need to be lost during a fractional vaporization hypothesis to reproduce the core:mantle ratio of present-day Mercury. In this work, we show that such high fractions of loss of silicate material are untenable, be it from a small or a large proto-Mercury (total mass losses are below 0.3%). The principal reason is that atmospheric cooling timescales are too rapid with respect to evaporation and escape timescales, meaning that integrated loss rates over $\sim 10^4$ yr are small with respect to the mass of proto-Mercury. Moreover, substantial amounts of atmospheric or collisional escape of Mercury's crust are not represented in the high K/U ratio of its surface (McCubbin et al. 2012), as preferential loss of silicate material will predominantly deplete its incompatible lithophile element budget (O'Neill & Palme 2008).

There are several caveats to our conclusions, namely, that our results are valid for dry or C- and H-bearing atmospheres but do not consider the effect of other minor volatiles (Cl, S, F) on the volatility behavior of metals. Metal chlorides and metal sulfides may be important gaseous species under moderate

temperatures (~1000 K; Renggli et al. 2017), increasing their volatility. Second, conditions on the surface of Mercury may have been considerably more reduced than modeled herein (IW-5; Cartier & Wood 2019). Because the partial pressures of most metal-bearing species increase with decreasing fO_2 (Equation (1)), vaporization rates for alkali metals may be an order of magnitude higher (considering that their exponent $n = 1/4$; Sossi et al. 2019).

However, these faster evaporation rates may be offset by the presence of a surficial graphite layer on the magma ocean (Keppler & Golabek 2019). Such a layer is promoted under reducing conditions as the solubility of C in silicate melt decreases from ~360 ppm at the IW buffer to 1 ppm at IW-4 (Duncan et al. 2017; Keppler & Golabek 2019). The extent of a graphite layer therefore depends on the C content of Mercury and its fO_2, both of which are poorly known. A surficial lid would additionally delay cooling of the mantle, unless the lid is regularly broken as possibly occurred for the flotation crust on the Moon (Perera et al. 2018). Nevertheless, the net effect of a graphite lid on Mercury's magma ocean would be to reduce the extent of degassing calculated herein. Therefore, we conclude that the physicochemical characteristics of Mercury cannot have been produced during a magma ocean stage on a near fully grown planet.

These obstacles are ameliorated when considering vapor loss from planetary building blocks. Should Mercury have accreted from smaller, kilometer-size planetesimals, then melting and vaporization on the precursor bodies would have led to more efficient mass loss (e.g., Hin et al. 2017). Thus, vaporization may still be a physically viable mechanism to explain Mercury's composition, provided that it occurred on its precursor bodies. However, another problem arises because moderately volatile elements, such as Na, S, and K, are always more volatile (i.e., their partial pressures are higher for a given activity) than the major mantle components, such as Mg and Si (Sossi et al. 2019). Moreover, as demonstrated herein, Na is more easily lost with respect to Mg and Si owing to its lower molar mass and higher tendency to remain in the gas phase in an adiabatically expanding atmosphere (Section 3.2.1). As such, appealing to evaporative loss of Mg and Si to increase the core:mantle ratio while retaining Na and K is inconsistent with evaporation from a silicate melt on small planetary bodies. Therefore, other hypotheses should be considered.

5. Conclusions

We combined chemical and thermodynamic equilibrium models of the thermal evolution of Mercury's magma ocean and gaseous species derived thereof, to model the thermochemical evolution of an early atmosphere on Mercury. For an initially large Hermean mantle with initial C and H budgets comparable to those of other rocky planets, namely, Earth ("volatile cases"), the lifetime of surficial melt may have reached almost 10^4 yr. Compared to a present-day-sized proto-Mercury without a greenhouse atmosphere, this lifetime is an order of magnitude larger and therefore may enable early atmospheric mass loss to occur over an extended duration. Cases with C and H show that Mercury could have started with a 5–12 bar atmosphere. By contrast, excluding the presence of C and H species results in a thin, short-lived metal- and metal-oxide-bearing atmosphere. The upper atmospheres of volatile cases are dominated by H_2 and CO, whereas nonvolatile cases are mostly Na and SiO.

Photoionization is a minor exospheric loss mechanism, limited by homopause diffusion ($\dot{M}_{\rm diff}$) up to a maximum of a few $\times 10^5$ kg s^{-1}. If C and H volatiles are absent from the atmosphere, the $\dot{M}_{\rm diff}$ limit applies to SiO and Na. Mass-loss rates via photoevaporation, $\dot{M}_U \leqslant 10^{9.5}$ kg s^{-1}, exceed those from all other known mechanisms owing to the high EUV luminosity of the early Sun. This could in the best-case scenario erode an equivalent thickness of up to 1 km of proto-Mercury's crust when assuming high EUV heating efficiencies of 10^{-1}. Atmospheric sputtering $\dot{M}_U \sim 10^{3.4}$ kg s^{-1} (also limited by $\dot{M}_{\rm diff}$) occurs at the exobase, knocking off neutral gas molecules owing to the ram pressure of the solar wind.

By integrating atmospheric loss rates over surficial melt lifetimes, we bracket the expected total mass loss from Mercury's early atmosphere. Based on photoionization, Jeans escape, and plasma heating, the evaporation and loss of the magma ocean of proto-Mercury did not significantly modify its bulk composition. This is because magma ocean cooling times are too short to drive substantial total loss for the determined atmospheric loss fluxes. Photoevaporation can remove an equivalent crustal thickness of up to 2.3 km in about 10,000 yr, which is approximately $\sim 10^{20}$ kg of material. Integrated losses of even the most volatile elements considered here, Na and K, are insignificant with respect to their total budgets when escape is diffusion limited (⩽0.02% decrease of the initial Na composition, which would be a difference of 3×10^{-4} wt%). Hence, the present Na-rich surface composition may indicate that catastrophic volatile loss during the magma ocean stage did not occur, and that Mercury's peculiar composition is inherited from that of the solar-proximal region of the nebula from which it accreted.

Financial support has been provided by the Swiss National Science Foundation (SNSF) Fund (200021L182771/1). D.J.B. acknowledges SNSF Ambizione grant 173992. P.A.S. was supported by SNSF Ambizione grant 180025, and A.W. by the National Science Foundation EAR 1725025, as well as the Turner Postdoctoral Fellowship. Thanks to S. Suriano, P. Saxena, A. Heays, S.-M. Tsai, and N. Ligterink for discussions relating to this work. Part of this work was conducted at the Jet Propulsion Laboratory, California Institute of Technology, under contract with NASA.

Appendix A
Magma Ocean Model

The evolving surface temperature of the Hermean magma ocean is calculated using the SPIDER code, which is described in detail in Bower et al. (2018, 2019, 2021). Table A1 shows the parameters used to model proto-Mercury. The mass absorption coefficients of H and C volatile species are determined at 1.01 bar, and the coefficients of SiO at 3×10^{-6} bar.

Table A1
Standard Parameters for Magma Ocean Cases

Parameter	Value	Units
Core heat capacity	850	$J\ kg^{-1}\ K^{-1}$
Core density	7200	$kg\ m^{-3}$
Core radius	2000	km
Equilibrium temperature, T_∞	440	K
Gravity, g	Table 1	$m\ s^{-2}$
Planetary radius, R_P	Table 1	km
Boundary layer scaling, b	10^{-7}	K^{-2}
Al abundance[a]	19500	ppmw
$^{26}Al/Al$ (zero time)	5.25×10^{-5}	…
K abundance[b]	403	ppmw
$^{40}K/K$ (present time)	1.17×10^{-4}	…
Th abundance[b]	49	ppbw
$^{232}Th/Th$ (present time)	1	…
U abundance[b]	28	ppbw
$^{235}U/U$ (present time)	0.007	…
$^{238}U/U$ (present time)	0.993	…
H_2 mass absorption (CIA)	5×10^{-5} [d]	$m^2\ kg^{-1}$
H_2 solubility law		
H_2O mass absorption	10^{-2} [e]	$m^2\ kg^{-1}$
H_2O solubility law		
CO mass absorption	10^{-5} [d]	$m^2\ kg^{-1}$
CO solubility law		
CO_2 mass absorption	10^{-4} [e]	$m^2\ kg^{-1}$
CO_2 solubility law		
SiO mass absorption (large)	10^{-3}	$m^2\ kg^{-1}$
SiO mass absorption (small)	10^{-5}	$m^2\ kg^{-1}$
Initial surface temperature	2400[c]	K

Notes.
[a] Average Al abundance based on the composition of EH4 and NSP source (Table 2).
[b] Average current estimates for bulk heat source from Tosi et al. (2013) and natural abundances from Ruedas (2017).
[c] Similar to maximum temperature estimate of Mercury's surface during accretion and differentiation (Bhatia & Sahijpal 2017).
[d] Lichtenberg et al. (2021).
[e] Bower et al. (2019).

Appendix B
VapoRock Species

The species included in VapoRock are given in Table B1.

Table B1
Species Included in VapoRock (Wolf et al. 2021)

Species					
Al	AlO	AlO_2	Al_2	Al_2O	Al_2O_2
Si	SiO	SiO_2	Si_2	Si_2O_2	Si_3
K	KO	KO_2	K_2	K_2O	
Na	NaO	Na_2	Na_2O		
Mg	MgO	Mg_2			
Ca	CaO	Ca_2			
Fe	FeO				
O	O_2				

Appendix C
Modified Vulcan

We incorporated Na, Si, Mg, K, Fe, and their derivatives into VULCAN by adding 12 reactions (from kinetics.nist.gov) to the preexisting chemistry network based on C, H, and O (Table C1). We initially added more reactions but removed those that had a negligible impact on the resulting atmospheric speciation when omitted.

Table C1
Key Reactions Added to VULCAN

Reaction		
$OH + SiO$	$\rightarrow$	$SiO_2 + H$
$OH + Si$	$\rightarrow$	$SiO + H$
$Si + O_2$	$\rightarrow$	$SiO + O$
$NaO + O$	$\rightarrow$	$Na + O_2$
$Na + H_2O$	$\rightarrow$	$NaOH + H$
$H_2O + NaO$	$\rightarrow$	$NaOH + OH$
$H_2 + NaO$	$\rightarrow$	$NaOH + H$
$HCO + Na$	$\rightarrow$	$CO + NaH$
$Mg + O_2$	$\rightarrow$	$MgO + O$
$H_2O + KO$	$\rightarrow$	$KOH + OH$
$CO_2 + Fe$	$\rightarrow$	$CO + FeO$
Three-body Reactions		
$OH + K + M$	$\rightarrow$	$KOH + M$
$Na + O_2 + M$	$\rightarrow$	$NaO_2 + M$
$NaOH + M$	$\rightarrow$	$OH + Na + M$
$FeO + H_2O + M$	$\rightarrow$	$Fe(OH)_2 + M$

Note. The reactions given affect the speciation of Si, Mg, Fe, Na, K, and Si in the ranges $T = 2000$–873 K and $P = 11.7$–10^{-7} bar.

Appendix D
Collision Cross Sections

The CCSs are shown in Table D1, which were approximated by the circular area of radius equal to the atom or bond length. Furthermore, all bonds were approximated to be covalent.

Table D1
Species Cross Sections (CS) Used

Species	CS (Å^2)	Species	CS (Å^2)
H	0.88	CO_2	10.3
H_2	1.29	KOH	19.6
H_2O	2.84	Na	11.3
O	1.13	K	18.6
O_2	4.08	SiO	8.45
C	1.41	Mg	6.61
CO	4.01	Fe	7.65

Note. CS values are based on sizes of atomic, single-bond, double-bond, and triple-bond data (Clementi et al. 1967; Pyykkö & Atsumi 2009a, 2009b; Pyykkö et al. 2005).

Appendix E
Atmospheric *P–T* Profile

SPIDER determines an atmospheric pressure–temperature profile through an analytical solution to the radiative transfer equations (see Appendix in Abe & Matsui 1985 and Section 3.7.2 in Andrews 2010). The solution gives rise to the skin temperature equation (Equation (7)). Figure E1 shows the volatile (V) and nonvolatile (N3, N5) atmospheric pressure–temperature profiles that are used for FactSage and VULCAN calculations. An unphysical outcome of assuming only radiative equilibrium (no convection) is a temperature discontinuity between the base of the atmosphere and the surface of the magma ocean, which is visually more evident for the nonvolatile cases that have a small optical depth. Nevertheless, for all cases the surface temperature is 2000 K.

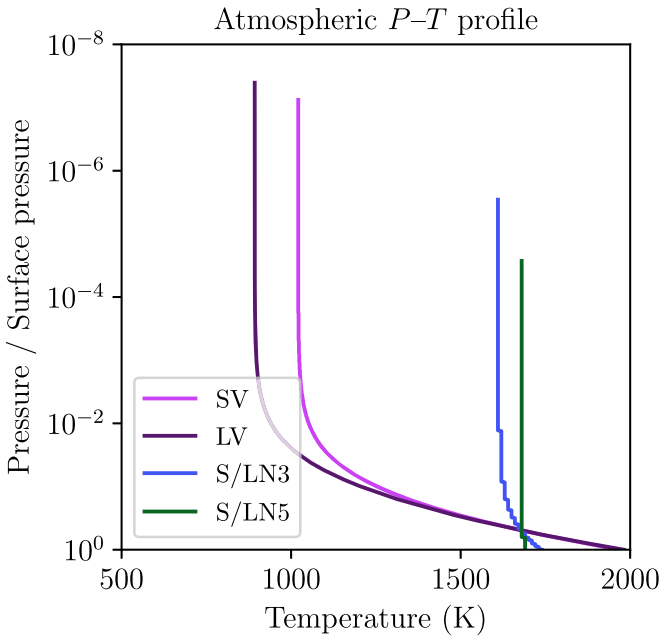

Figure E1. Atmospheric *P–T* profiles of the volatile (V) and nonvolatile (N3, N5) atmospheres surrounding a small (S) and large Mercury. The LN3 and LN5 profiles are omitted, as they are visually indistinguishable from the respective S case profiles.

ORCID iDs

Noah Jäggi https://orcid.org/0000-0002-2740-7965
Diana Gamborino https://orcid.org/0000-0002-7019-6286
Dan J. Bower https://orcid.org/0000-0002-0673-4860
Paolo A. Sossi https://orcid.org/0000-0002-1462-1882
Aaron S. Wolf https://orcid.org/0000-0003-2415-0508
Apurva V. Oza https://orcid.org/0000-0002-1655-0715
Audrey Vorburger https://orcid.org/0000-0002-7400-9142
André Galli https://orcid.org/0000-0003-2425-3793
Peter Wurz https://orcid.org/0000-0002-2603-1169

References

Abe, Y., & Matsui, T. 1985, JGRB, 90, C545
Aiuppa, A., Dongarrà, G., Valenza, M., Federico, C., & Pecoraino, G. 2003, GMS, 139, 41
Andrews, D. G. 2010, An Introduction to Atmospheric Physics (2nd ed.; Cambridge: Cambridge Univ. Press)
Asphaug, E., & Reufer, A. 2014, NatGe, 7, 564
Atreya, S. K., Sandel, B. R., Romani, P. N., et al. 1986, BAAS, 18, 758
Bale, C. W. 2016, Calphad: Computer Coupling of Phase Diagrams and Thermochemistry, 55, 1
Benz, W., Anic, A., Horner, J., & Whitby, J. A. 2008, Mercury, Space Sciences Series of ISSI, Vol. 26 (Berlin: Springer), 7
Benz, W., Slattery, W. L., & Cameron, A. 1988, Icar, 74, 516
Bhatia, G. K., & Sahijpal, S. 2017, M&PS, 52, 295
Bird, G. A. 1994, Molecular Gas Dynamics And The Direct Simulation Of Gas Flows (Berlin: Springer)
Bouvier, L. C., Costa, M. M., Connelly, J. N., et al. 2018, Natur, 558, 586
Bower, D. J., Hakim, K., Sossi, P. A., & Sanan, P. 2021, PSJ, submitted (arXiv:2108.01790)
Bower, D. J., Kitzmann, D., Wolf, A. S., et al. 2019, A&A, 631, A103
Bower, D. J., Sanan, P., & Wolf, A. S. 2018, PEPI, 274, 49
Brown, S. M., & Elkins-Tanton, L. T. 2009, E&PSL, 286, 446
Cartier, C., & Wood, B. J. 2019, Elements, 15, 39
Cassidy, T. A., McClintock, W. E., Killen, R. M., et al. 2016, GeoRL, 43, 11,121
Chao, K.-H., deGraffenried, R., Lach, M., et al. 2021, Geoch, 81, 125735
Chapman, S., & Cowling, T. G. 1970, The Mathematical Theory of Non-uniform Gases: An Account of the Kinetic Theory of Viscosity, Thermal Conduction and Diffusion in Gases (Cambridge: Cambridge Univ. Press)
Charlier, B., Grove, T. L., & Zuber, M. T. 2013, E&PSL, 363, 50
Chau, A., Reinhardt, C., Helled, R., & Stadel, J. 2018, ApJ, 865, 35
Clementi, E., Raimondi, D. L., & Reinhardt, W. P. 1967, JChPh, 47, 1300
Duncan, M. S., Dasgupta, R., & Tsuno, K. 2017, E&PSL, 466, 115
Egan, H., Jarvinen, R., Ma, Y., & Brain, D. 2019, MNRAS, 488, 2108
Elkins-Tanton, L. 2008, E&PSL, 271, 181
Elkins-Tanton, L. T. 2012, AREPS, 40, 113
Evans, L. G., Peplowski, P. N., McCubbin, F. M., et al. 2015, Icar, 257, 417
Fegley, B., & Cameron, A. G. W. 1987, E&PSL, 82, 207
Gamborino, D., Vorburger, A., & Wurz, P. 2019, AnGp, 37, 455
Gebek, A., & Oza, A. V. 2020, MNRAS, 497, 5271
Genda, H., & Abe, Y. 2003, Icar, 164, 149
Ghiorso, M. S., & Sack, R. O. 1995, CoMP, 119, 197
Gronoff, G., Arras, P., Baraka, S., et al. 2020, JGRA, 125, e27639
Grott, M., Breuer, D., & Laneuville, M. 2011, E&PSL, 307, 135
Hin, R. C., Coath, C. D., Carter, P. J., et al. 2017, Natur, 549, 511
Humayun, M., & Cassen, P. 2000, Origin of the Earth and Moon (Tucson, AZ: Univ. Arizona Press), 3
Hyodo, R., Genda, H., & Brasser, R. 2021, Icar, 354, 114064
Ito, Y., & Ikoma, M. 2021, MNRAS, 502, 750
Ito, Y., Ikoma, M., Kawahara, H., et al. 2015, ApJ, 801, 144
Johnson, R. E. 1990, Energetic Charged-Particle Interactions with Atmospheres and Surfaces (Berlin: Springer)
Johnson, R. E. 2004, ApJL, 609, L99
Johnson, R. E., Oza, A., Young, L. A., Volkov, A. N., & Schmidt, C. 2015, ApJ, 809, 43
Johnstone, C. P., Güdel, M., Brott, I., & Lüftinger, T. 2015, A&A, 577, A28
Keppler, H., & Golabek, G. 2019, Geochemical Perspectives Letters, 11, 12
Kim, Y. K., & Desclaux, J. P. 2002, PhRvA, 66, 012708
Korth, H., Anderson, B. J., Johnson, C. L., et al. 2012, JGRA, 117, A00M07
Krenn, A. F., Fossati, L., Kubyshkina, D., & Lammer, H. 2021, A&A, 650, A94
Kruijer, T. S., Touboul, M., Fischer-Gödde, M., et al. 2014, Sci, 344, 1150
Lamoreaux, R. H., & Hildenbrand, D. L. 1984, JPCRD, 13, 151
Lamoreaux, R. H., Hildenbrand, D. L., & Brewer, L. 1987, JPCRD, 16, 419
Lauretta, D. S., Goreva, J. S., Hill, D. H., & Killgore, M. 2007, LPSC, 38, 2236
Lellouch, E., Belton, M., De Pater, I., et al. 1992, Icar, 98, 271
Lellouch, E., Paubert, G., Moses, J. I., Schneider, N. M., & Strobel, D. F. 2003, Natur, 421, 45
Lewis, J. S. 1972, E&PSL, 15, 286
Lichtenberg, T., Bower, D. J., Hammond, M., et al. 2021, JGRE, 126, e06711
McCoy, T. J., Peplowski, P. N., McCubbin, F. M., & Weider, S. Z. 2018, in Mercury: The View after MESSENGER, ed. S. C. Solomon, L. R. Nittler, & B. J. Anderson (Cambridge: Cambridge Univ. Press), 176
McCubbin, F. M., Riner, M. A., Vander Kaaden, K. E., & Burkemper, L. K. 2012, GeoRL, 39, L09202
Mordasini, C. 2020, A&A, 638, A52
Moullet, A., Gurwell, M. A., Lellouch, E., & Moreno, R. 2010, Icar, 208, 353
Murray-Clay, R. A., Chiang, E. I., & Murray, N. 2009, ApJ, 693, 23
Namur, O., Collinet, M., Charlier, B., et al. 2016, E&PSL, 439, 117
Nittler, L. R., Starr, R. D., Weider, S. Z., et al. 2011, Sci, 333, 1847
Nittler, L. R., & Weider, S. Z. 2019, Elements, 15, 33

O'Neill, H. S. C., & Eggins, S. M. 2002, ChGeo, 186, 151
O'Neill, H. S. C., & Palme, H. 2008, RSPTA, 366, 4205
Oza, A. V., Johnson, R. E., Lellouch, E., et al. 2019, ApJ, 885, 168
Peplowski, P. N., Evans, L. G., Stockstill-Cahill, K. R., et al. 2014, Icar, 228, 86
Perera, V., Jackson, A. P., Elkins-Tanton, L. T., & Asphaug, E. 2018, JGRE, 123, 1168
Pyykkö, P., & Atsumi, M. 2009a, CEJ, 15, 186
Pyykkö, P., & Atsumi, M. 2009b, CEJ, 15, 12770
Pyykkö, P., Riedel, S., & Patzschke, M. 2005, CEJ, 11, 3511
Renggli, C. J., King, P. L., Henley, R. W., & Norman, M. D. 2017, GeCoA, 206, 296
Renggli, C. J., & Klemme, S. 2020, JVGR, 400, 106929
Ribas, Á., Merín, B., Bouy, H., & Maud, L. T. 2014, A&A, 561, A54
Ruedas, T. 2017, GGG, 18, 3530
Semenov, D., Henning, T., Helling, C., Ilgner, M., & Sedlmayr, E. 2003, A&A, 410, 611
Siegfried, R. W., & Solomon, S. C. 1974, Icar, 23, 192
Sossi, P. A., & Fegley, B. 2018, RvMG, 84, 393
Sossi, P. A., Klemme, S., O'Neill, H. S., Berndt, J., & Moynier, F. 2019, GeCoA, 260, 204
Spohn, T. 1991, Icar, 90, 222
Stevenson, D. J. 1990, in Origin of the Earth, ed. H. E. Newsom & J. H. Jones (New York: Oxford Univ. Press), 231
Stevenson, D. J., Spohn, T., & Schubert, G. 1983, Icar, 54, 466
Thomas, N., Bagenal, F., Hill, T. W., & Wilson, J. K. 2004, in Jupiter: the planet, satellites and magnetosphere, ed. F. Bagenal, T. E. Dowling, & W. B. McKinnon, Vol. 1 (Cambridge: Cambridge Univ. Press), 561
Tosi, N., Grott, M., Plesa, A.-C., & Breuer, D. 2013, JGRE, 118, 2474
Tsai, S.-M., Lyons, J. R., Grosheintz, L., et al. 2017, ApJS, 228, 20
Tsai, S.-M., Malik, M., Kitzmann, D., et al. 2021, arXiv:2108.01790
Tu, L., Johnstone, C. P., Güdel, M., & Lammer, H. 2015, A&A, 577, L3
Tucker, O. J., Killen, R. M., Johnson, R. E., & Saxena, P. 2021, Icar, 359, 114304
Vander Kaaden, K. E., & McCubbin, F. M. 2016, GeCoA, 173, 246
Visscher, C., & Fegley, B. 2013, ApJL, 767, 12
Vlasov, M. N., & Kelley, M. C. 2015, AnGeo, 33, 857
Volkov, A. N., & Johnson, R. E. 2013, ApJ, 765, 90
Vorburger, A., Wurz, P., Lammer, H., Barabash, S., & Mousis, O. 2015, Icar, 262, 14
Watson, A. J., Donahue, T. M., & Walker, J. C. G. 1981, Icar, 48, 150
Weidenschilling, S. J. 1978, Icar, 35, 99
Weisberg, M. K., Prinz, M., Clayton, R. N., et al. 2000, M&PS, 36, 401
Weisberg, M. K., Prinz, M., & Nehru, C. E. 1990, Metic, 25, 269
Wiik, H. B. 1956, GeCoA, 9, 279
Wolf, A. S., Jäggi, N., Sossi, P. A., Bower, D. J., & Ghiorso, M. S. 2021, VapoRock: Thermodynamics of vaporized silicate rocks & melts for modeling magma ocean atmospheres and stellar nebula, v0.1, Zenodo doi:10.5281/zenodo.4594226
Wurz, P., & Lammer, H. 2003, Icar, 164, 1